



Article

Cite this article: Liu C, Hao G, Li Y, Zhao J, Lei R, Cheng B, Gao Z, Yang Q (2022). The sensitivity of parameterization schemes in thermodynamic modeling of the landfast sea ice in Prydz Bay, East Antarctica. *Journal of Glaciology* 68(271), 961–976. <https://doi.org/10.1017/jog.2022.8>

Received: 16 April 2021

Revised: 22 January 2022

Accepted: 24 January 2022

First published online: 17 March 2022

Keywords:


Antarctic landfast sea ice; oceanic heat flux; parameterization schemes; sensitivity tests; thermodynamically modeling

Author for correspondence:

Qinghua Yang,

E-mail: yangqh25@mail.sysu.edu.cn

The sensitivity of parameterization schemes in thermodynamic modeling of the landfast sea ice in Prydz Bay, East Antarctica

Changwei Liu¹, Guanghua Hao², Yubin Li³, Jiechen Zhao⁴, Ruibo Lei⁵ , Bin Cheng⁶ , Zhiqiu Gao^{3,7} and Qinghua Yang¹ 

¹School of Atmospheric Sciences, Sun Yat-sen University, and Southern Marine Science and Engineering Guangdong Laboratory (Zhuhai), Zhuhai, China; ²National Marine Environmental Forecasting Center, Ministry of Natural Resources, Beijing, China; ³Collaborative Innovation Center on Forecast and Evaluation of Meteorological Disasters, School of Atmospheric Physics, Nanjing University of Information Science and Technology, Nanjing, China; ⁴Harbin Engineering University Qingdao Graduate School, Qingdao Innovation and Development Center (Base) of Harbin Engineering University, Qingdao, China; ⁵Key Laboratory for Polar Science of the MNR, Polar Research Institute of China, Shanghai 200136, China; ⁶Finnish Meteorological Institute (FMI), Helsinki, Finland and ⁷State Key Laboratory of Atmospheric Boundary Layer Physics and Atmospheric Chemistry, Institute of Atmospheric Physics, Chinese Academy of Sciences, Beijing, China

Abstract

Based on the measurements conducted over the landfast sea ice in Prydz Bay, East Antarctica during the sea-ice growth season in 2016, various parameterization schemes in the high-resolution thermodynamic snow/ice model HIGHTSI are evaluated. The parameterization scheme of turbulent fluxes produces the largest errors compared with the parameterization schemes for other surface heat fluxes. However, the sea-ice thickness simulation is most sensitive to the differences in upward longwave radiation at the surface. In addition, the sea-ice thickness simulation during the growth season is highly sensitive to the oceanic heat flux, and a new oceanic heat flux parameterization scheme based on the bulk method is proposed. The new parameterization scheme is tested in a second year, and it significantly improves the model performance relative to the standard configuration when compared against observations. Finally, the seasonal variation in the heat budget and its influence on the sea-ice thickness variation are analyzed. The net short-wave radiation, sensible heat flux and conductive heat flux (the net longwave radiation and latent heat flux) are found to be the surface heat sources (heat sinks) during the growth season. The larger conductive heat flux and the smaller oceanic heat flux can intensify the growth of sea ice.

1. Introduction

The response of the variation in Antarctic sea ice to global climate change has attracted increasing attention in recent decades. However, researchers still struggle to understand the mechanism responsible for the variation in Antarctic sea ice at the interannual scale, and current climate models exhibit an unsatisfactory performance when simulating Antarctic sea-ice variations (Turner and Comiso, 2017; Shu and others, 2020). As an important component of the Antarctic climate system, landfast sea ice accounts for 35% (5%) of the total Antarctic sea-ice extent in summer (winter) (Fraser and others, 2012). In East Antarctica, the contribution of landfast sea ice to the sea-ice mass balance is greater than the drifting sea ice (Giles and others, 2008). The existence of landfast sea ice can reduce the energy exchange between the ocean and atmosphere, thereby affecting the regional atmospheric circulation and ecosystem.

Thermodynamic processes dominate the annual evolutionary cycle of landfast sea-ice thickness (h_{si}) because of its immobility (Dumas and others, 2005). Accordingly, some previous studies have tested the sensitivity of the evolution of the Antarctic landfast sea-ice thickness to various thermodynamic processes using thermodynamic numerical models. For example, Heil and others (1996) concluded that the sea-ice evolution is most sensitive to the oceanic heat flux, snow cover and albedo. In contrast, Yang and others (2016a) pointed out that the albedo is important in summer and that snow cover plays a minor role in Prydz Bay because of the effect of redistribution by wind. By comparing the evolution of first-year sea ice with that of second-year sea ice in a small scale (~ 10 km) landfast sea-ice zone, Zhao and others (2017) found that the conductive heat flux led to the differences in the evolution of first- and second-year sea ice because of the differences in sea-ice thickness. Nevertheless, although the sensitivities of some thermodynamic processes were tested in these studies by altering the corresponding parameterization scheme to force the model, evaluations of the parameterization schemes of thermodynamic processes remain limited due to the scarcity of observations, especially for the observations of turbulence and radiation fluxes over the sea ice; hence, the influence of the differences between parameterized and observed parameters on the simulation of sea-ice mass balance need to be better understood.

In particular, due to the sparsity of oceanic heat flux observations, the oceanic heat flux is the least documented parameter in thermodynamic studies of sea ice. In the Arctic, an oceanic heat flux of 2 W m^{-2} is widely considered a reasonable annual basin-averaged value during

© The Author(s), 2022. Published by Cambridge University Press. This is an Open Access article, distributed under the terms of the Creative Commons Attribution-NonCommercial-NoDerivatives licence (<https://creativecommons.org/licenses/by-nc-nd/4.0/>), which permits non-commercial re-use, distribution, and reproduction in any medium, provided the original work is unaltered and is properly cited. The written permission of Cambridge University Press must be obtained for commercial re-use or in order to create a derivative work.

winter (Maykut and Untersteiner, 1971). In Antarctica, reference values were obtained via model tuning with sea-ice thickness observations (Gordon and Huber, 1990; Heil and others, 1996; Lei and others, 2010; Yang and others, 2016a; Zhao and others, 2019). Heil and others (1996) suggested that the oceanic heat flux varied from 5 to 12 W m⁻² within a full sea-ice season for the landfast sea ice off Mawson station. In Prydz Bay, East Antarctica, Lei and others (2010) demonstrated that the oceanic heat flux derived based on the heat balance at the sea-ice bottom decreased from 11.8 W m⁻² in April to 1.9 W m⁻² in September; in contrast, Yang and others (2016a) reported that the oceanic heat flux decreased from 25 to 5 W m⁻² during the growth season and recovered back to 25 W m⁻² in summer. The oceanic heat flux shows a seasonal variation and some potential interannual changes. However, without sea-ice mass-balance measurements, it is difficult to quantitatively determine the oceanic heat flux, and thus, how to present a reasonable parameterization scheme for the oceanic heat flux in numerical models remains a topic of ongoing research.

Prydz Bay in East Antarctica is one of the local sites from which intensive observations have been acquired. There are four operational year-round stations within or surrounding Prydz Bay: Davis, Zhongshan, Progress II and Mawson, which makes the contribution of this region to the Antarctic landfast sea-ice monitoring network being particularly important. Previous studies concluded that the annual maximum first-year landfast sea-ice thickness ranged from 1.5 to 1.8 m and decreased to <1.0 m before break-up, while the maximum second-year landfast sea-ice thickness could even exceed 3 m in this region (Heil, 2006; Tang and others, 2006; Lei and others, 2010; Yang and others, 2016a, 2016b). In 2016, comprehensive observations were conducted over the landfast sea ice near Zhongshan station. High-quality datasets, especially turbulence fluxes over the sea ice, have been collected for the first time at this location (Liu and others, 2020). These datasets provide an excellent opportunity to evaluate the thermodynamic parameterization schemes in numerical models.

Therefore, focusing on the thermodynamic processes of the landfast sea ice near Zhongshan station, this study aims to evaluate the thermodynamic parameterization schemes and further investigate the sensitivity of parameterization schemes to sea-ice thickness simulation in the sea-ice thermodynamic model. Furthermore, we attempt to identify a reasonable parameterization scheme for the oceanic heat flux. The data and methods are described in Section 2. Then, the results and discussion are presented in Section 3. Finally, the conclusions are given in Section 4.

2. Data and methods

2.1 Site and instruments

The observation site was located on landfast sea ice along the coast of Prydz Bay, East Antarctica, at 69°22′08.1″S 76°21′42.1″E (Fig. 1a). During the observation campaign from 29 April to 31 October in 2016, a mast was put up on the sea ice to measure meteorological parameters (Hao and others, 2020). The instruments setup on the mast included (Fig. 1b): an HMP155 air temperature and humidity sensor (Vaisala Inc., Finland), a CS106 barometer (Vaisala Inc., Finland), a CNR4 net radiometer (Kipp & Zonen Inc., the Netherlands), an in situ, open-path, mid-infrared gas (CO₂/H₂O) analyzer integrated with a 3-D sonic anemometer (IRGASON, Campbell Sci. Inc., USA) and an SR50A sonic distance sensor used for snow depth (h_s) measurement (Campbell Sci. Inc., USA). However, the SR50A sensor was broken after 1 September 2016, so the snow depth was measured manually once per day from then onward. Additionally, the cloudiness at Zhongshan station was observed visually every 6 h,

the daily accumulated precipitation was measured at Russian Progress II station (located ~1 km from Zhongshan station), and the sea-ice thickness and sea-water temperature beneath the sea-ice bottom were recorded manually by borehole measurements about once a week, and the positions of measurements were very close to the observation site. The sea-water temperature was measured using a Cond 3210 SET1 (Xylem Inc., Germany) sensor during the sea-ice thickness measurement. To derive one record of sea-ice thickness at least three repeat measurements were made, and these three measurements were made on the same core. The uncertainty of measured sea-ice thickness is $\sim\pm 0.005$ m. This is a low-end estimate of the sea-ice thickness uncertainty, which originates from the variability between cores. The key technical specifications and installation information of these instruments are summarized in Table 1. The meteorological data were first published in Liu and others (2020), and the data processing and quality control procedures were the same as those in Liu and others (2020), while the sea-ice data are first presented in this study. We consider the positive heat fluxes as the surface or sea-ice bottom gains the energy, while the negative heat fluxes indicate the surface or bottom loses energy in this study.

2.2 Sea-ice model

2.2.1 Model description and initial setup

The growth and ablation of landfast sea ice are controlled mainly by thermodynamic processes (Williams and others, 2014). Hence, in this study, to simulate the landfast sea-ice mass balance, we choose a vertical 1-D thermodynamic snow and sea-ice model, i.e. the high-resolution thermodynamic snow/ice (HIGHTSI) model (Launiainen and Cheng, 1998). To date, this model is widely used as a tool to investigate the influence of sea-ice properties or synoptic process on the simulation of sea-ice mass balance in the Antarctica and Arctic (Cheng and others, 2013; Zhao and others, 2017; Merkouriadi and others, 2017, 2020). The main thermodynamic processes and corresponding parameterization schemes, as well as their initial settings included in the HIGHTSI model are summarized in Table 2. Five input variables wind speed (U), air temperature (T_a), relative humidity (R_h), cloudiness (C_n) and precipitation (P) were initially used to force the model. Note that HIGHTSI does not consider the effects of blowing snow on the snow depth, even though blowing snow may play an important role in local snow accumulation. Hence, to eliminate the uncertainty of the snow depth simulation, we use the observed snow depth instead of precipitation to force the model. The initial sea-ice thickness and snow depth input for modeling are 0.53 and 0.23 m, respectively, which are observed on 29 April 2016.

As shown in Fig. 2a, the maximum 6 hourly averaged wind speed attains 13.7 m s⁻¹, and the mean wind speed is 4.1 m s⁻¹. The mean air temperature is -16.8°C, and the 6 hourly averaged maximum and minimum air temperatures are -1.6 and -47.1°C, respectively (Fig. 2b). For the surface temperature, which is derived from measured longwave radiation with the Stefan-Boltzmann relation (e.g. Vihma and others, 2009; Yang and others, 2016b), the mean value is -18.6°C. The 6 hourly averaged maximum and minimum surface temperatures are -3.8 and -47.8°C, respectively (Fig. 2b). The half-hourly averaged surface temperature is first observed to attain 0°C on 31 October. It is noted that the surface temperature refers to the surface skin temperature regardless of the bare sea-ice surface or snow surface. For the relative humidity (Fig. 2c), the mean value is 57.1%. Figure 2d shows the variation in cloudiness observed visually every 6 h. For the whole observation period, the proportions of $C_n \leq 0.1$ and $C_n \geq 0.9$ are 38.1 and 44.0%, respectively. Since the time step of the

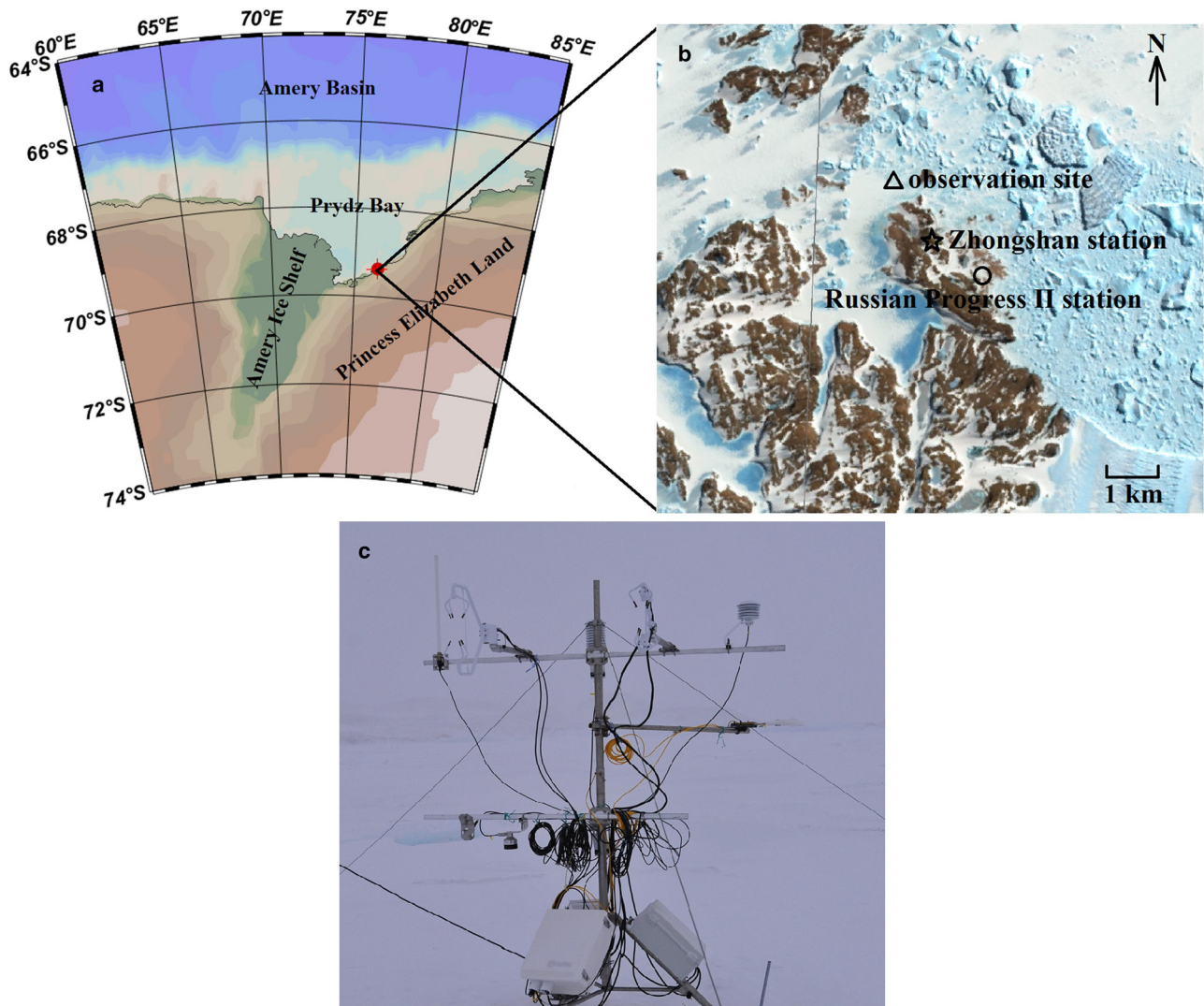


Fig. 1. (a) Geographical location of the observation site (red dot), (b) the local topography and (c) the meteorological tower at the observation site.

Table 1. Key technical specifications and installation information of the sensors

Sensor type	Measurement range	Precision	Sampling frequency (Hz)	Installation height (m)
HMP155	T_a : -80 to +60°C R_h : 0.8–100%	$\pm(0.226 - 0.0028 \times T_a)$ °C in -80 to +20°C $\pm(1.2 + 0.012 \times R_h)$ % in -40 to -20°C $\pm(1 + 0.008 \times R_h)$ % in -20 to +40°C	0.1	2
CS106	P_a : 500–1100 hPa	± 1.5 hPa in -40 to +60°C	0.1	0.5
CNR4	Shortwave: 0.3–2.8 μm Longwave: 4.5–42 μm	Daily totals: $\pm 10\%$	0.1	1.5
IRGASON	u : -30 to +30 m s ⁻¹ v : -60 to +60 m s ⁻¹ w : -8 to +8 m s ⁻¹ T_{sonic} : -50 to +60°C q : 0–72 mmol mol ⁻¹	u, v : ± 0.08 m s ⁻¹ w : ± 0.04 m s ⁻¹ T_{sonic} : ± 0.025 °C q : ± 0.006 mmol mol ⁻¹	10	2
SR50A	h_s : 0–10 m	± 0.001 m	0.1	1
Cond 3210 SET1 (manually deployed)	T_{os} : -5 to +105°C	± 0.1 °C	Once a week	~0.1

HIGHTSI model is set to 30 min in this study, we interpolate the observed cloudiness every 6 h in half-hour increments. Figure 2e describes the variation in snow depth. The snow depth is maintained at ~0.2 m before heavy precipitation occurred on 11 July, due to which the snow depth sharply increases to a maximum of 0.67 m; then, the snow depth gradually decreases until 15 August. From 1 September to 31 October, the accumulated snow shows a slight decreasing trend, and the snow depth attains

0.12 m at the end of the observation period. As shown in Fig. 2e, the precipitation is concentrated in June (25.0 mm) and July (44.1 mm), and the maximum daily precipitation of 19.2 mm occurred on 11 July.

2.2.2 Design of controlled trials

To evaluate the parameterization schemes of different thermodynamic processes in the HIGHTSI model, we directly compare

Table 2. Various parameterization schemes that can be used in the HIGHTSI model

Thermodynamic parameter	Parameterization schemes	Initial settings
Solar radiation (Q_s)	Sh84 scheme (Shine, 1984)	-
Albedo (α)	PW79 scheme (Parkinson and Washington, 1979)	Pe96 scheme
	SMHI scheme (Vancoppenolle and others, 2009)	
	HIRHAM scheme (Dethloff and others, 1996)	
	REMO scheme (Jacob and others, 2001)	
	HadCM3 scheme (Gordon and others, 2000)	
	FB96 scheme (Flato and Brown, 1996)	
	ARCSYM scheme (Lynch and others, 1995)	
	CCSM3 scheme (Briegleb and others, 2004)	
	Pe96 scheme (Perovich, 1996)	
Downward longwave radiation (Q_d)	Ku61 scheme (Kuzmin, 1961)	Gu98 scheme
	Ef61 scheme (Efimova, 1961)	
	Sw63 scheme (Swinbank, 1963)	
	IJ69 scheme (Idso and Jackson, 1969)	
	MC73 scheme (Maykut and Church, 1973)	
	Br75 scheme (Brustaert, 1975)	
	Sa79 scheme (Satterlund, 1979)	
	Oh81 scheme (Ohmura, 1981)	
	Id81 scheme (Idso, 1981)	
	AA82 scheme (Andreas and Ackley, 1982)	
	Pr96 scheme (Prata, 1996)	
	Gu98 scheme (Guest, 1998)	
Upward longwave radiation (Q_b)	Stefan-Boltzmann law	-
Sensible heat flux (Q_h) and latent heat flux (Q_{le})	Bulk method (Launiainen and Cheng, 1995)	-
Thermal conductivity of snow (k_i)	St97 scheme (Sturm and others, 1997)	-
Thermal conductivity of sea ice (k_s)	MU71 scheme (Maykut and Untersteiner, 1971)	-
Oceanic heat flux (Q_w)	15 W m ⁻² (Yang and others, 2016a)	-

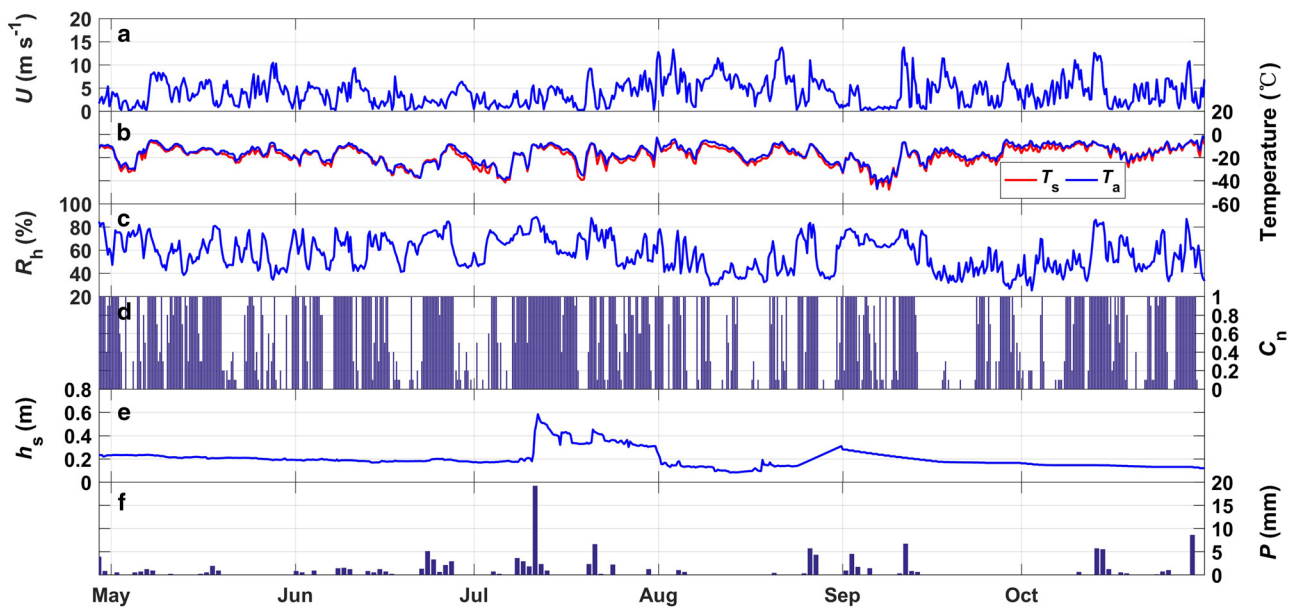


Fig. 2. Time series of the observed 6 hourly averaged (a) wind speed, (b) air temperature, (c) relative humidity, (d) cloudiness, (e) snow depth and (f) daily precipitation during the whole observation period.

the results of solar radiation (Q_s), albedo (α), downward longwave radiation (Q_d), upward longwave radiation (Q_b), sensible heat flux (Q_h) and latent heat flux (Q_{le}) from parameterization schemes with the corresponding observations. Then, we analyze the sensitivities of the simulation of sea-ice thickness to the differences between the parameterizations and observations through controlled trials. In the control groups, all the thermodynamic processes in the HIGHTSI model are described by parameterization schemes. In the experimental groups, we prescribe (rather than parameterizing) one variable using our observations to force the model. For example, to evaluate the influence of the differences between the parameterized and observed solar radiation on the sea-ice thickness simulation, we compare the simulation results from the HIGHTSI model forced by observed U , T_a , R_h ,

C_n and h_s (the control group) with those forced by observed U , T_a , R_h , C_n , h_s and Q_s (the experimental group). Analogously, the design of the other control trials is described in Table 3. It should be noted that we use observed snow depth to force the model, the effects of thermodynamic processes on snow melting will be ignored, which may affect the reliability of sensitivity tests. However, during the sea-ice growth season the influence of thermodynamic processes on determining snow depth is negligible and the conclusion drawn from sensitivity studies by using observed snow depth will not be unreliable because of eliminating the feedback of thermodynamic processes on snow depth. In addition, to further understand the effects of the oceanic heat flux on the sea-ice thickness simulation, we compare the simulation results with different oceanic heat flux values, i.e. exp. F1 ($Q_w =$

Table 3. Design of the controlled trials

Factor	Design of the control group	Design of the experimental group
Q_s	Observed forcing: U, T_a, R_h, C_n, h_s Parameterized forcing: Sh84 (exp. A1) Other parameterized forcing: default	Observed forcing: $U, T_a, R_h, C_n, h_s, Q_s$ Other parameterized forcing: default
α	Observed forcing: U, T_a, R_h, C_n, h_s Parameterized forcing: PW79 (exp. B1), SMHI (exp. B2), HIRHAM (exp. B3), REMO (exp. B4), HadCM3 (exp. B5), FB96 (exp. B6), ARCSYM (exp. B7), CCSM3 (exp. B8), Pe96 (exp. B9) Other parameterized forcing: default	Observed forcing: $U, T_a, R_h, C_n, h_s, \alpha$ Other parameterized forcing: default
Q_d	Observed forcing: U, T_a, R_h, C_n, h_s Parameterized forcing: Ku61 (exp. C1), Ef61 (exp. C2), Sw63 (exp. C3), IJ69 (exp. C4), MC73 (exp. C5), Br75 (exp. C6), Sa79 (exp. C7), Oh81 (exp. C8), Id81 (exp. C9), AA82 (exp. C10), Pr96 (exp. C11), Gu98 (exp. C12) Other parameterized forcing: default	Observed forcing: $U, T_a, R_h, C_n, h_s, Q_d$ Other parameterized forcing: default
Q_b	Observed forcing: U, T_a, R_h, C_n, h_s Parameterized forcing: Stefan-Boltzmann law (exp. D1) Other parameterized forcing: default	Observed forcing: $U, T_a, R_h, C_n, h_s, Q_b$ Other parameterized forcing: default
Q_h and Q_{le}	Observed forcing: U, T_a, R_h, C_n, h_s Parameterized forcing: bulk method (exp. E1) Other parameterized forcing: default	Observed forcing: $U, T_a, R_h, C_n, h_s, Q_h, Q_{le}$ Other parameterized forcing: default
Q_w	Observed forcing: U, T_a, R_h, C_n, h_s Parameterized forcing: 5 W m^{-2} (exp. F1), 15 W m^{-2} (exp. F2), 25 W m^{-2} (exp. F3) Other parameterized forcing: default	-
k_c	Observed forcing: $U, T_a, R_h, C_n, h_s, Q_s, \alpha, Q_d, Q_b, Q_h, Q_{le}, Q_w$ (exp. G) Parameterized forcing: range from 0 to $50 \text{ W m}^{-2} \text{ } ^\circ\text{C}^{-1}$ with a step of $0.1 \text{ W m}^{-2} \text{ } ^\circ\text{C}^{-1}$	-

5 W m^{-2}), exp. F2 ($Q_w = 15 \text{ W m}^{-2}$) and exp. F3 ($Q_w = 25 \text{ W m}^{-2}$). These values of Q_w are in the typical range of Q_w reported by previous studies in Antarctica (Gordon and Huber, 1990; Heil and others, 1996; Lei and others, 2010; Yang and others, 2016a; Zhao and others, 2019).

2.3 Calculations of sea-ice thickness in the HIGHTSI model

The total sea-ice thickness change is determined by the sea-ice evolution at the surface and bottom. At the surface, the melting dominated the change of snow or sea-ice thickness, and it can be expressed as (Launiainen and Cheng, 1998):

$$Q_m = -\rho_i L_f \left(\frac{dh_{si}}{dt} \right)_{sur}, \tag{1}$$

where Q_m is the excess energy consider to melt the snow or sea ice when the surface temperature exceeds the melting point, ρ_i is the sea-ice density, L_f is the latent heat of freezing and $(dh_{si}/dt)_{sur}$ is the snow or sea-ice thickness change at the surface.

At the sea-ice bottom, the sea-ice thickness change can be calculated as:

$$-\rho_i L_f \left(\frac{dh_{si}}{dt} \right)_{bot} = \left(-k_i \left(\frac{\partial T_i}{\partial z} \right)_{bot} + Q_w \right), \tag{2}$$

where $(dh_{si}/dt)_{bot}$ is the sea-ice thickness change at the bottom, k_i is the thermal conductivity of sea-ice, $(\partial T_i/\partial z)_{bot}$ is the temperature gradient at the bottom and Q_w is the oceanic heat flux. Finally, the total sea-ice thickness change $(dh_{si}/dt)_{tot}$ can be derived according to:

$$\left(\frac{dh_{si}}{dt} \right)_{tot} = \left(\frac{dh_{si}}{dt} \right)_{sur} + \left(\frac{dh_{si}}{dt} \right)_{bot}. \tag{3}$$

2.4 Parameterizing the oceanic heat flux

In the HIGHTSI model, the ocean mixed-layer model is not included and the oceanic heat flux is set as a constant. However, some previous studies reported that the oceanic heat flux in the

landfast sea-ice zone in Antarctica exhibited significant seasonal variation (Heil and others, 1996; Lei and others, 2010; Yang and others, 2016a; Zhao and others, 2019). Hence, we consider presenting a modified parameterization scheme for the oceanic heat flux. The oceanic heat flux can be accurately expressed as:

$$Q_w = \rho_s c_{ps} \langle w'_s T'_{os} \rangle, \tag{4}$$

where ρ_s and c_{ps} ($= 3980 \text{ J kg}^{-1} \text{ K}^{-1}$, Ackley and others, 2015) are the density and specific heat capacity of sea water respectively, and $\langle w'_s T'_{os} \rangle$ is the vertical turbulent heat flux of sea water, which can be obtained by using acoustic Doppler velocimetry combined with conductivity, temperature and depth measurements. However, we had not measured ocean turbulence or velocity below the sea ice. To obtain the Q_w without turbulent measurements, McPhee and others (1999) used the bulk method to estimate $\langle w'_s T'_{os} \rangle$:

$$\langle w'_s T'_{os} \rangle = C_{Hs} u_{0*} (T_{os} - T_w), \tag{5}$$

where C_{Hs} is the bulk transfer coefficient for heat in the sea, and the reference value is 0.0057 (Kirillov and others, 2015); T_{os} and T_w are the sea-water temperature beneath the sea ice and the temperature of the sea-ice bottom, respectively, where T_w is set as -1.8°C according to Heil and others (1996); u_{0*} is the frictional velocity beneath the sea ice. For the landfast sea ice, the quadratic resistance law can be used to describe the relationship between u_{0*} and the velocity of sea water (U_s) according to Jenkins and others (2010):

$$u_{0*}^2 = c_w U_s^2, \tag{6}$$

where c_w is a dimensionless drag coefficient, and the reference value is 0.0055 (Hibler, 1979). Unfortunately, we lack the observations on U_s . To simply optimize the oceanic heat flux without U_s observations in the HIGHTSI model, we suppose that:

$$Q_w = k_c (T_{os} - T_w), \tag{7}$$

where k_c is the empirical coefficient. As shown in Eqns (4–6), k_c should be related to the current velocity, density and heat capacity of sea water. In this study, k_c is assumed to be a constant. To determine the best possible value of k_c , the HIGHTSI model is ran with

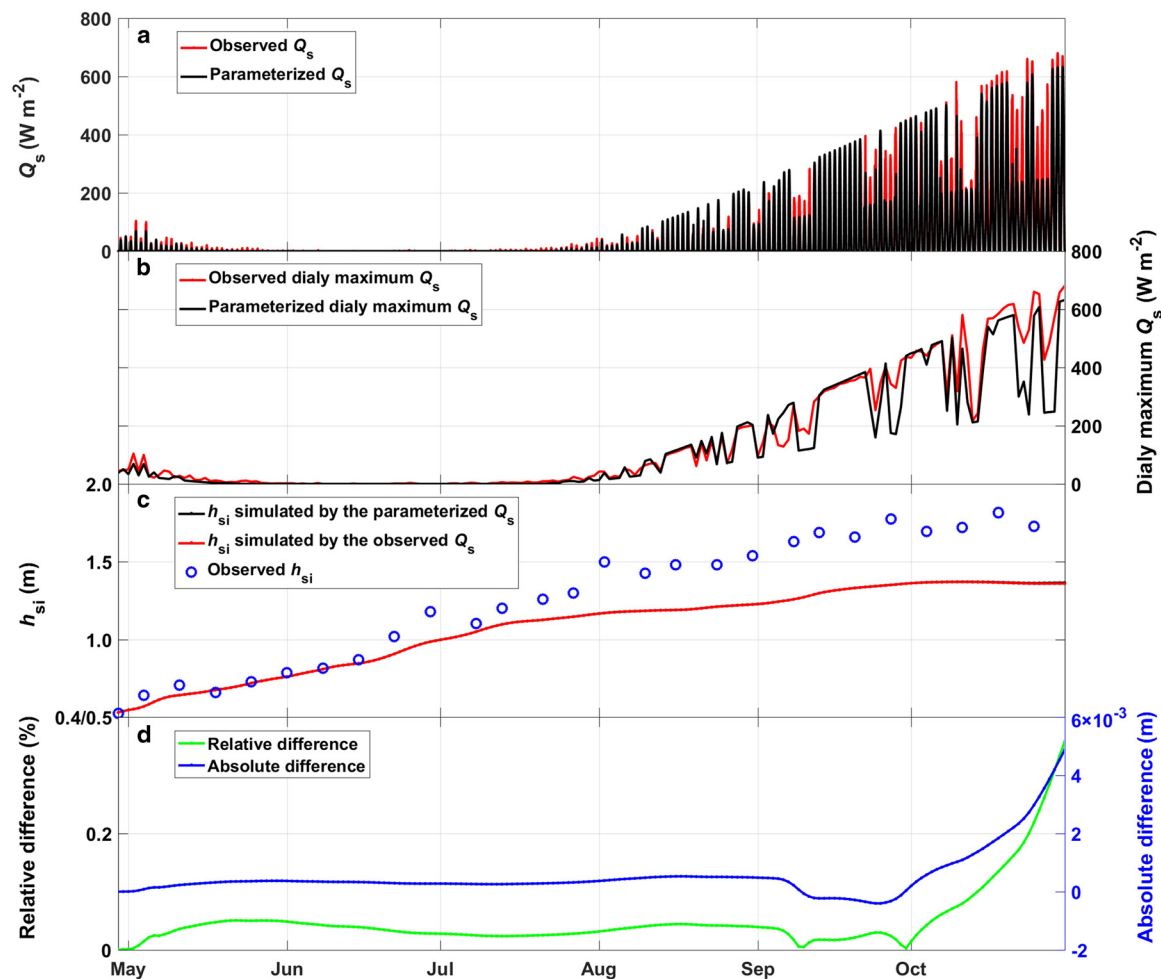


Fig. 3. Comparison of the (a) solar radiation and (b) daily maximum solar radiation between the observed (red line) and parameterized (black line) results, (c) the comparison among observed sea-ice thickness (blue dots), simulated sea-ice thickness by the parameterized solar radiation (black line) and that by the observed solar radiation (red line) and (d) the differences between the sea-ice thickness simulated by the parameterized solar radiation and that simulated by the observed solar radiation.

a step of $0.1 \text{ W m}^{-2} \text{ }^{\circ}\text{C}^{-1}$ within the range from 0 to $50 \text{ W m}^{-2} \text{ }^{\circ}\text{C}^{-1}$ of k_c . It should be noted that all the surface thermodynamic processes are prescribed based on the observations in these experiments. Then the optimal value of k_c can be identified when the minimum bias between the modeled and observed sea-ice thicknesses is obtained. Hence, k_c is a tuning parameter.

3. Results and discussion

3.1 Evaluation of the solar radiation parameterization scheme

In the HIGHTSI model, the Q_s parameterization scheme for a clear sky was proposed by Shine (1984), and a cloudiness factor of $(1 - 0.52C_n)$ is used for cloudy conditions (Bennett, 1982). As shown in Fig. 3a, the parameterization scheme of Q_s can accurately reproduce the observations during the period from May to September when the Q_s is relatively small. However, the parameterized Q_s is underestimated in some periods after September. This is partially caused by the uncertainty in the visually observed cloudiness because it is observed at Zhongshan station, $\sim 1 \text{ km}$ away from our sea-ice measurement site. In addition, the using of empirical cloudiness factor of $(1 - 0.52C_n)$ may be another cause for the underestimation of Q_s , for example, the cloudiness factor of $(1 - 0.6C_n^3)$ proposed by Parkinson and Washington (1979) produces larger solar radiation reaching to the surface when $C_n < 0.94$. Figure 3b presents the observed and parameterized daily maximum Q_s , revealing that the

parameterized daily maximum Q_s is underestimated after mid-October.

To quantitatively understand the influence of the differences between the parameterized and observed Q_s on the sea-ice thickness simulation, Fig. 3c compares the sea-ice thickness simulated by the parameterized Q_s with that simulated by the observed Q_s , which the results demonstrate are very similar to each other. As shown in Fig. 3d, the relative difference, defined as the ratio of the difference between the sea-ice thickness simulated by the parameterized Q_s and that simulated by the observed Q_s to the sea-ice thickness simulated by the observed Q_s (a similar definition is used for the following variables), is $< 0.1\%$ before October but increases to a maximum of 0.36% at the end of October. While the absolute difference, defined as the sea-ice thickness simulated by the parameterized Q_s minus the sea-ice thickness simulated by the observed Q_s (a similar definition is used for the following variables), does not exceed $6 \times 10^{-3} \text{ m}$ during the whole observation period. These results indicate that the effects of the differences between the parameterized Q_s and observed Q_s on the sea-ice thickness simulation are negligible in the HIGHTSI model during the observation period.

Figure 3c also presents the observed sea-ice thicknesses obtained by borehole measurements. The observed sea-ice thickness is 0.53 m at the beginning of the observation period and gradually grows to a maximum of 1.82 m by 18 October 2016. Comparing with the simulated sea-ice thickness by the HIGHTSI model under initial settings (equivalent to the sea-ice

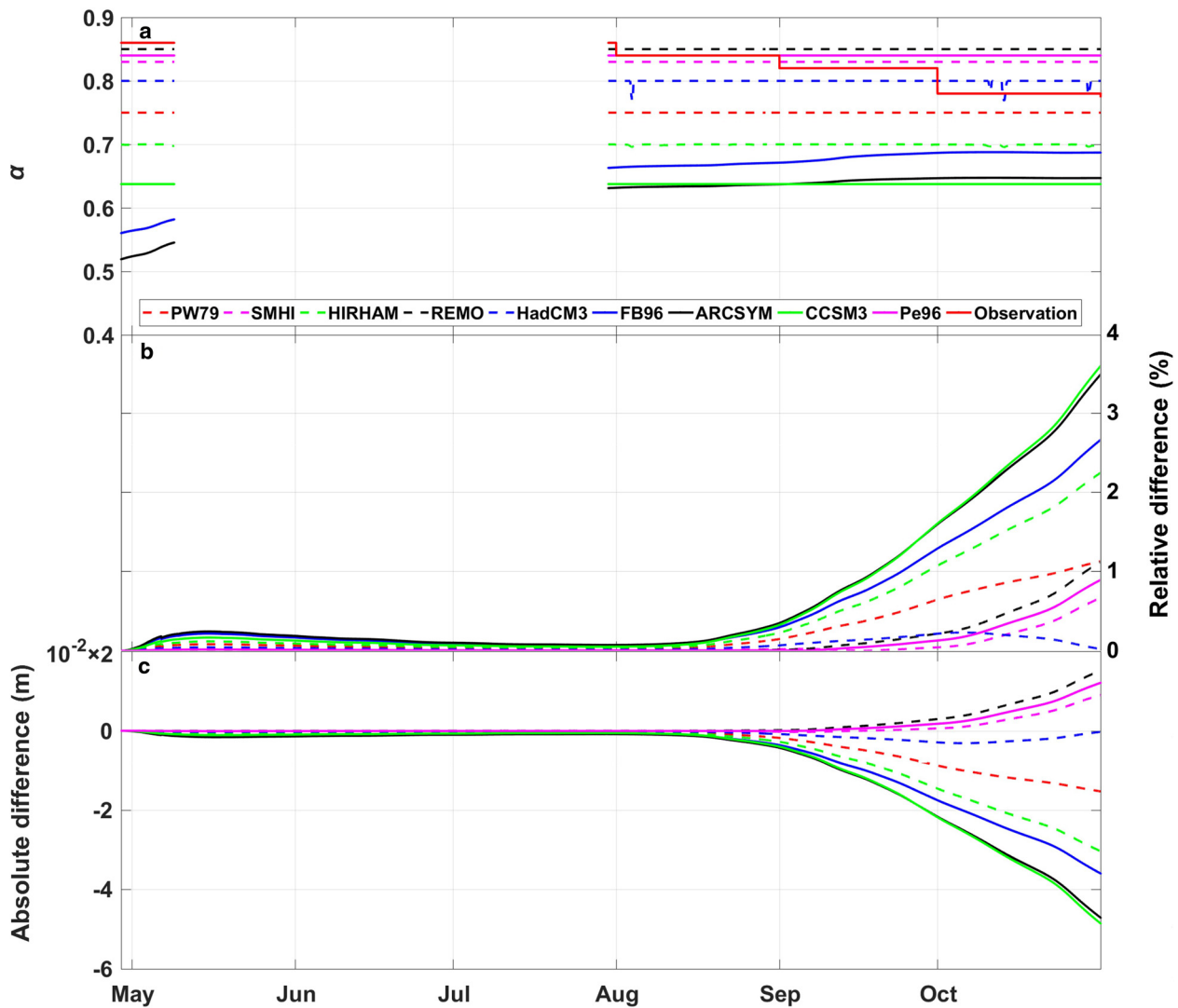


Fig. 4. Comparison of albedo between the observed and parameterized results, and (b) the relative differences and (c) absolute differences in the sea-ice thickness simulated using various albedo parameterization schemes against that simulated using the observed albedo.

thickness simulated by the parameterized Q_s), it is clear that the simulation results are consistent with observations before mid-June, but they are significantly underestimated after mid-June. The differences between the simulation results and observations tend to increase with time.

3.2 Evaluation of albedo parameterization schemes

There are nine parameterization schemes for α in the HIGHTSI model (as shown in Table 2). Figure 4a presents the parameterized α and the observed monthly mean α when the observed daily maximum $Q_s > 20 \text{ W m}^{-2}$. The std dev. of observed monthly mean albedo is ~ 0.06 for each month. According to the variation in the observed monthly mean α , the maximum of 0.86 appears before August 2016, and the observed monthly mean α gradually decreases from July to October, which is related to the metamorphism of the snow cover. Moreover, the parameterization result of 0.86 from the REMO scheme is more consistent with the observations before August compared with those from the other schemes; however, in August and September, the Pe96 scheme and SMHI scheme perform better, respectively, and the HadCM3 scheme performs better than the other schemes in October. Generally, the current version of the HIGHTSI model cannot accurately describe the seasonal variation in α over snow surface by using a single parameterization scheme.

Furthermore, we examine the influence of the parameterized α on the sea-ice thickness simulation. Figures 4b, c present the relative differences and the absolute differences in the sea-ice thickness simulated using different α parameterization schemes compared with that simulated using the observed α . The relative differences of all parameterization schemes are small before September but show considerable diversity after September. The relative differences of the CCSM3 scheme maintain a continuous increase after September, and the increase is the largest among all the schemes, attaining 3.5% at the end of the observation period. In contrast, the relative differences of the HadCM3 scheme are maintained at $< 0.3\%$ during the whole observation period, indicating that the HadCM3 scheme is the best choice for parameterizing α in the HIGHTSI model. It can also be found that the PW79, HIRHAM, HadCM3, FB96, ARCSYM and CCSM3 schemes produce negative absolute differences after September, while the absolute differences of SHMI, Perovich and REMO schemes are positive. In addition, Yang and others (2016a) concluded that the simulation of sea-ice thickness is very sensitive to the setting of the α parameterization scheme in the HIGHTSI model during the melting season. However, our results show relatively low sensitivity of the sea-ice thickness simulation to the α parameterization scheme because our experiment is carried out mainly during the growth season of sea ice, when Q_s is relatively small.

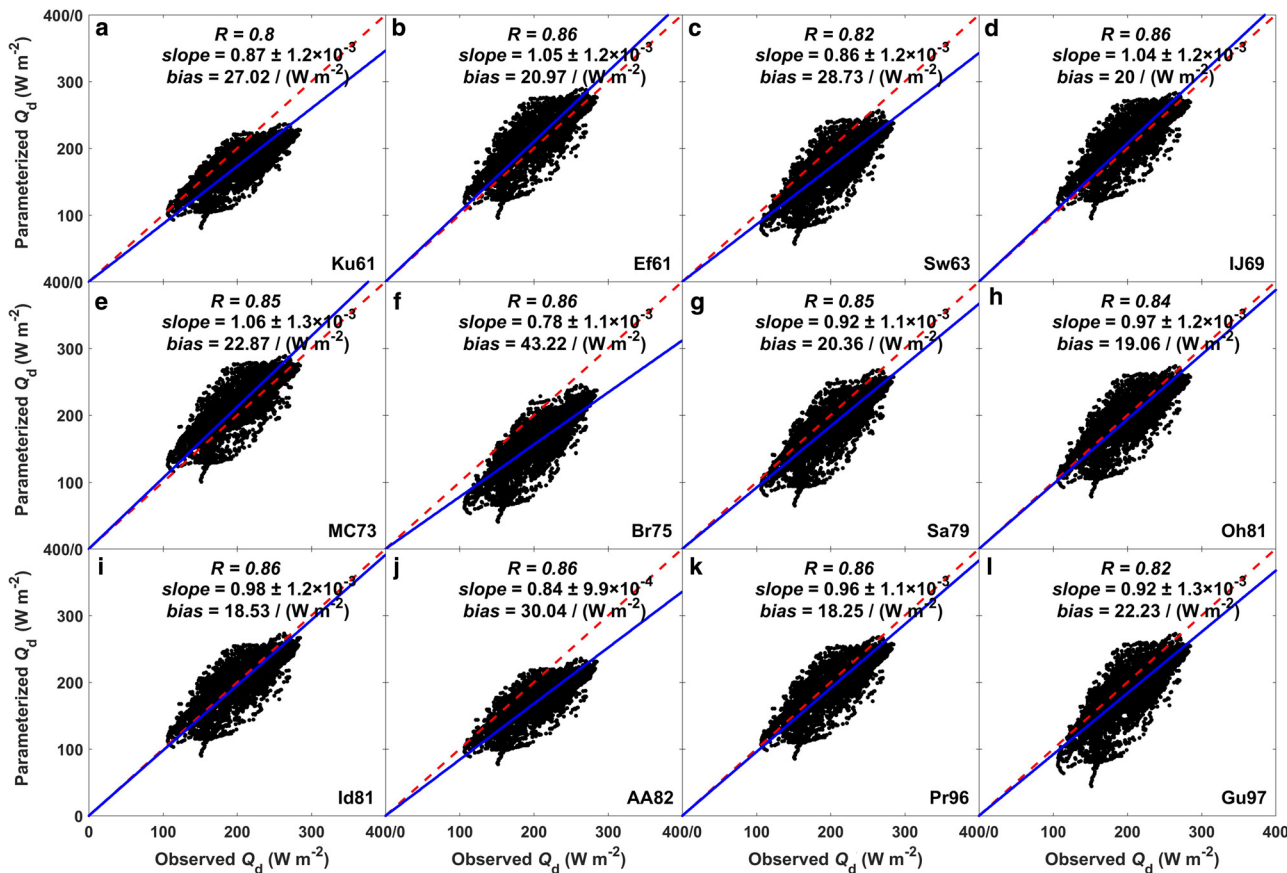


Fig. 5. Comparison between the observed atmospheric longwave radiation and parameterized atmospheric longwave radiation obtained using 12 different schemes. The red dotted line is the 1:1 line, and the blue solid line is the linear best-fitting line.

3.3 Evaluation of the longwave radiation parameterization schemes

The longwave radiation budget plays an important role in the surface heat balance, especially during winter when the shortwave radiation is relatively weak. However, the inaccuracy in estimating the atmospheric longwave radiation Q_d even under clear-sky conditions tends to be considerable (Launiainen and Cheng, 1998). In the HIGHTSI model, there are 12 parameterization schemes for determining Q_d . The cloudiness factor of $(1 + 0.26C_n)$ is used for cloudy conditions in Ef61, Sw63, Br75, Oh81, Id81, AA82, Pr96 and Gu97 schemes (Jacobs, 1978), and the cloudiness factors of $(1 + 0.12C_n)$, $(1 + 0.275C_n)$, $(1 + 0.2232C_n^{2.75})$ and $(1 + 0.2C_n^2)$ are used in Ku61, IJ69, MC73 and Sa79 schemes, respectively. Figure 5 compares the observed Q_d and parameterized Q_d obtained by these schemes. The *bias*, which is defined as $|\text{observed}Q_d - \text{parameterized}Q_d|/m$ (m is the number of samples), reflects the absolute difference between observations and parameterizations. Our results show that the Pr96 scheme produces the smallest *bias*, but the *bias* from the Br75 scheme is the largest. To evaluate the consistency of variation, the correlation coefficient (R) is also given in Fig. 5. It is found that the parameterizations based on the Ef61, IJ69, Br75, Id81, AA82 and Pr96 schemes show the highest correlation with observations, while the Ku61 scheme performs the worst. In addition, the *slope* is also used to quantify the systematic deviation. It can be found that the parameterizations from the Br75 scheme show the most significant underestimation, and the parameterizations from the Id85 scheme produce the smallest systematic deviation. By using the observations collected in the Arctic, Key and others (1996) also evaluated some Q_d parameterization schemes. They pointed that the Ef61 scheme for clear sky and the MC73 scheme for all-sky performed

well, but AA82 scheme was less accurate for clear sky. Similar results can also be reproduced in our assessment.

To further understand the influence of the differences between observed Q_d and parameterized Q_d on the sea-ice thickness simulation, Fig. 6 presents the relative differences in the sea-ice thicknesses simulated using various Q_d parameterization schemes against that simulated using the observed Q_d . As shown in Fig. 6a, the relative differences of the Id81 scheme are the smallest with an average of 0.5% during the whole observation period, whereas the relative differences derived from the Br75 scheme attain the maximum of 12.8%, and the average relative difference of the Br75 scheme (9.9%) is significantly higher than that of the other schemes. In addition, the Ef61, IJ69 and MC73 schemes present the negative absolute differences, while other schemes show the positive absolute differences. The Br75 (MC73) scheme produces the maximum positive (negative) absolute difference of 0.167 (−0.066) m at the end of the observation period. These results indicate that the choice of the Q_d parameterization scheme is important when simulating the sea-ice thickness in the HIGHTSI model, and the Id81 scheme appears to be more applicable for the landfast sea ice in the coastal region of East Antarctica.

The longwave radiation emitted from the snow/ice surface is determined using the Stefan–Boltzmann relation. In the HIGHTSI model, the surface temperature (T_s) is described by the surface heat balance equation:

$$F(T_s) = (1 - \alpha)Q_s - I_0 + Q_d - Q_b(T_s) + Q_h(T_s) + Q_{le}(T_s) + Q_c(T_s), \tag{8}$$

where $F(T_s)$ is the net flux, the term I_0 is the penetration part of solar radiation, and Q_c is the conductive heat flux. Under freezing

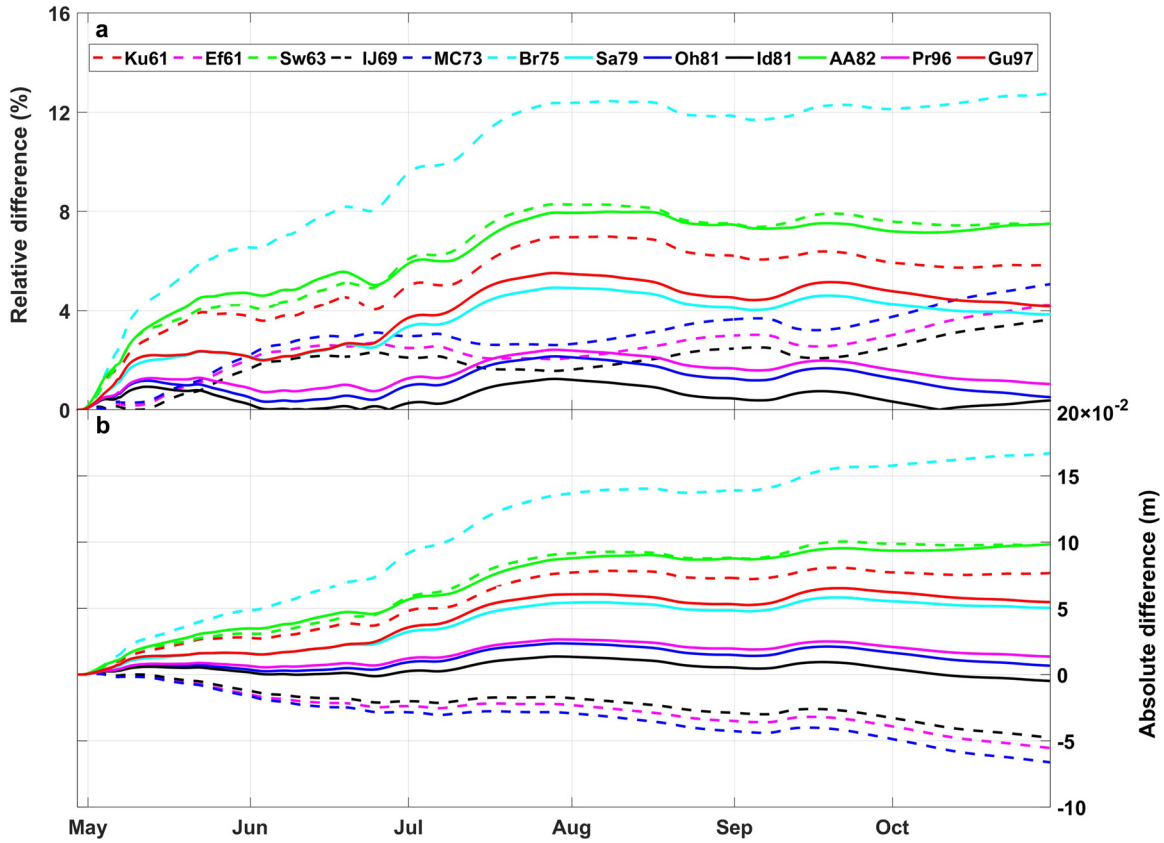


Fig. 6. (a) Relative differences and (b) absolute differences in the sea-ice thickness simulated using various atmospheric longwave radiation parameterization schemes against that simulated using the observed atmospheric longwave radiation.

conditions, $F(T_s)$ should be equal to 0 W m^{-2} . Then Eqn (8) can be solved effectively by the Newton iteration method (e.g. Launiainen and Cheng, 1998: refer to the HIGHTSI technical paper):

$$T_s^{n+1} = T_s^n - \frac{F(T_s^n)}{F'(T_s^n)}, \quad n = 0, 1, 2, 3 \dots \quad (9)$$

where $F'(T_s^n)$ denotes the derivative term with respect to T_s . T_s^0 is the first guess of T_s , which is set as $T_a - 0.5^\circ\text{C}$. Then, the iterative processes are made to match $|T_s^{n+1} - T_s^n| < 0.01$, and the maximum iterative step is set to be 15 (i.e. $n = 15$). Once the value of T_s is obtained, the corresponding Q_b can also be derived by the Stefan-Boltzmann relation. Figure 7 compares the calculated Q_b with the observed Q_b , demonstrating that the calculated Q_b is fractionally underestimated compared with the observed Q_b . The bias, R and slope between the calculated Q_b and observed Q_b are 13.5 W m^{-2} , 0.82 and 0.98, respectively.

On the other hand, the observed Q_b can be used as an input to force the HIGHTSI model; in this case, the term related to Q_b in $F(T_s)$ should be eliminated. Figure 8 compares the sea-ice thickness simulated using the parameterized Q_b against that simulated using the observed Q_b , revealing that the former is generally larger than the latter, and the differences between them gradually increase during the sea-ice growth season. The mean relative difference (absolute difference) during the whole observation period is 5.4% (0.06 m), and the maximum relative difference (absolute difference) can attain 7.5% (0.09 m). In the HIGHTSI model, T_s plays an important role in simulating sea-ice thickness because it not only determines the surface melting but also directly affects the snow and sea-ice temperature profiles. Although the surface melting can be ignored during the sea-ice growth season, the

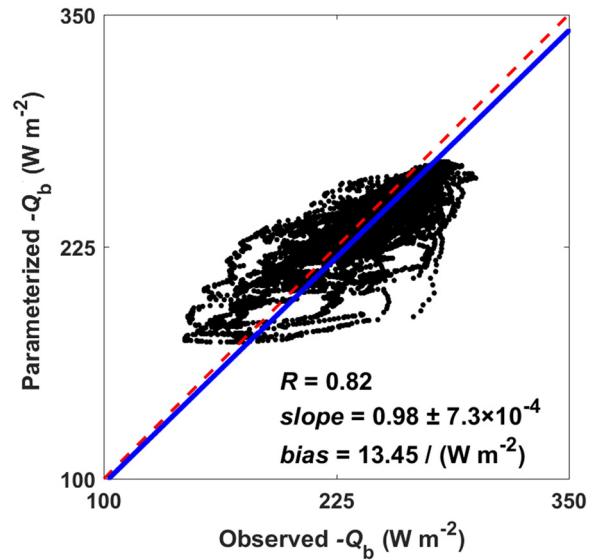


Fig. 7. Comparison between the observed upward longwave radiation and calculated upward longwave radiation. The red dotted line is the 1:1 line, and the blue solid line is the linear best-fitting line.

impacts of surface temperature on snow and sea-ice temperature profiles cause the differences of simulated sea-ice thickness by different parameterization schemes. The differences between parameterized Q_b and observed Q_b produce the relatively large differences in the calculated surface temperature, which further lead to the relatively large differences in the simulated sea-ice thickness. Furthermore, our results also show that the simulated sea-ice thickness is sensitive to the differences between

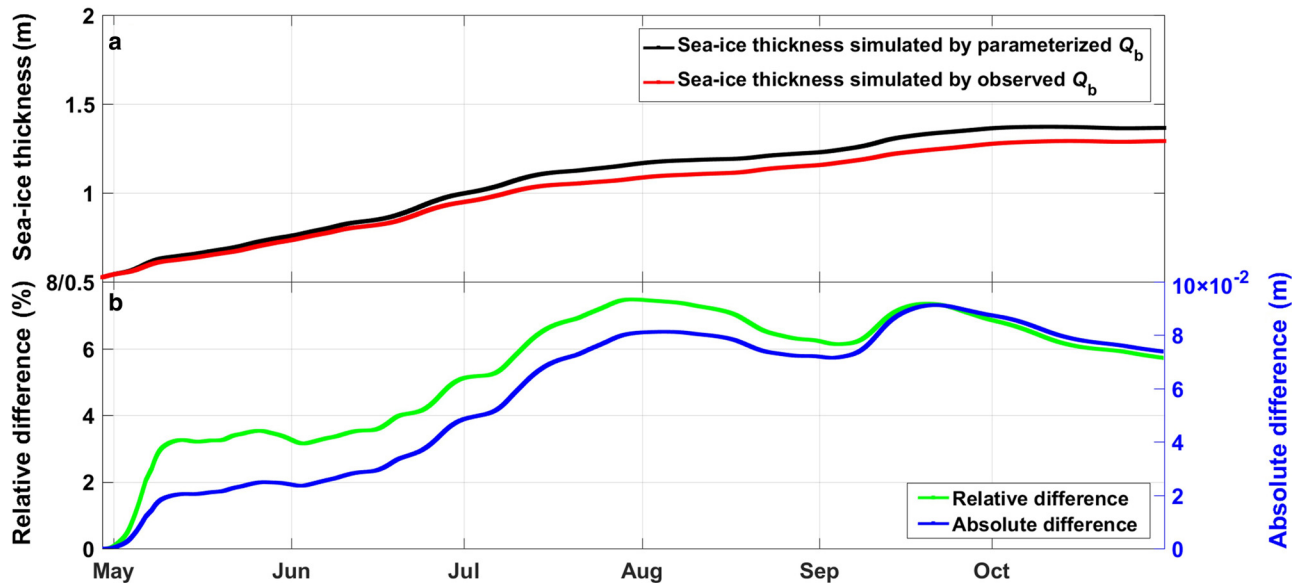


Fig. 8. (a) Sea-ice thickness simulated using the parameterized upward longwave radiation (black line) and that simulated using the observed upward longwave radiation (red line) and (b) their relative (green line, scaled to the left y axis) and absolute (blue line, scaled to the right y axis) differences.

parameterized Q_b and observed Q_b at the upper sea-ice boundary. This may indicate that the using of observed Q_b instead of parameterized Q_b induces the significant influence on the calculation of surface temperature.

3.4 Evaluation of the turbulent heat flux parameterization schemes

In the HIGHTSI model, Q_h and Q_{le} are parameterized using the familiar bulk formula based on the Monin–Obukhov similarity (MOS) theory; the details of the calculation can be found in Launiainen and Cheng (1998). The settings of the aerodynamic roughness length (z_{0m}) and scalar roughness length for temperature (z_{0h}) in the HIGHTSI model follow Banke and others (1980) and Andreas (1987). The z_{0m} calculated by Banke and others (1980) is 1.42×10^{-4} m, and the z_{0h} ranges from 1.1×10^{-8} to 1.6×10^{-4} m according to Andreas (1987). However, Liu and others (2020) analyzed the same dataset employed in this study and revealed that the values of z_{0m} and z_{0h} should be 1.9×10^{-3} and 3.7×10^{-5} m, respectively. Hence, the values of z_{0m} and z_{0h} in the HIGHTSI model are revised according to Liu and others (2020). Figures 9a, b compare the parameterized Q_h and Q_{le} against the corresponding observations, revealing that Q_h is overestimated by the HIGHTSI model, whereas Q_{le} is underestimated. The accuracies of the parameterized Q_h and Q_{le} are greatly inferior compared with the parameterization results of the radiation fluxes in the HIGHTSI model. For Q_h , we further analyze why the parameterization result is markedly overvalued with the same z_{0m} and z_{0h} as employed by Liu and others (2020). We find that the underestimation of the calculated surface temperature in the HIGHTSI model is the main cause of the overvalued Q_h . Thus, if we use the observed T_s to calculate Q_h with the same method as described in the HIGHTSI model, the parameterized Q_h is consistent with the observations (as shown in Fig. 9c). For Q_{le} , the inaccuracy may be related to the uncertainty in the surface humidity and the corresponding roughness length in the parameterization scheme. However, effective means with which to measure these key parameters are lacking. Hence, because of problems with identifying parameters and their availability, there is still an imperfection in parameterizing Q_{le} within the MOS theory framework.

Furthermore, to quantify the influence of the differences between the parameterized and observed surface turbulent heat fluxes (Q_h and Q_{le}) on the sea-ice thickness simulation, we compare the sea-ice thickness simulated by the parameterized Q_h and Q_{le} with that simulated by the observed Q_h and Q_{le} in Fig. 10, demonstrating that the latter is slightly thinner than the former. The maximum relative difference is only 5.5%, and the mean relative difference is 3.1%. For absolute differences, the maximum value of 0.05 m occurs in mid-July and mid-September and the mean absolute difference is 0.03 m. In addition, although the parameterized surface turbulent heat fluxes show a large discrepancy compared with observations, the influence of the differences between the parameterized and observed surface turbulent heat fluxes on the sea-ice simulation is smaller than that of the differences between the parameterized and observed Q_b on the sea-ice simulation.

3.5 Sensitivity test and improvement of the oceanic heat flux parameterization scheme

In the HIGHTSI model, Q_w is initially set as a constant. However, Q_w is highly dependent on the sea-water temperature, salinity and current velocity beneath the sea-ice bottom (Kirillov and others, 2015). Hence, a proper determination of Q_w may necessitate coupling an ocean mixed-layer model. In the current study, we first test the sensitivity of Q_w to the sea-ice thickness simulation during the growth season. Figure 11 shows the simulated sea-ice thicknesses obtained by expts. F1, F2 and F3. The simulated sea-ice thicknesses clearly vary with different values of Q_w , and the differences tend to increase with time. The simulated maximum sea-ice thickness is 1.1 m when using Q_w of 25 W m^{-2} ; however, it can attain 1.73 m when Q_w is 5 W m^{-2} . This result indicates that the sea-ice thickness simulation is very sensitive to Q_w during the sea-ice growth season. Thus, it is crucial to accurately describe Q_w in the HIGHTSI model.

Furthermore, we derive a more reasonable Q_w parameterization scheme by running the HIGHTSI model with the observed heat fluxes at the upper sea-ice boundary. As demonstrated in Section 2.4, a simple bulk formula is adopted to determine Q_w . Figure 12a presents the observed $T_{os} - T_w$ retrieved by borehole measurements, which are acquired at a frequency of

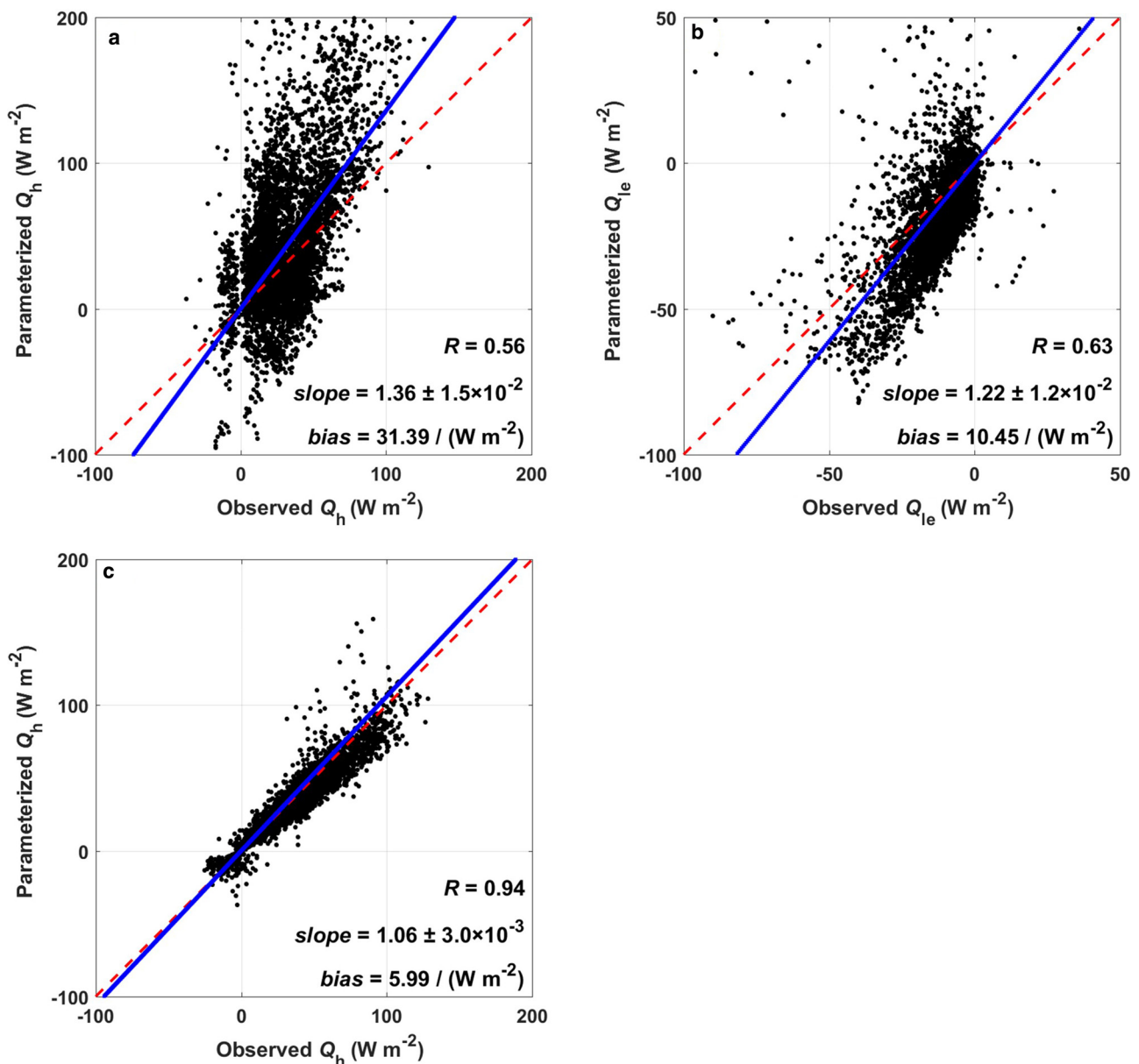


Fig. 9. Comparison of the parameterized (a) sensible heat flux and (b) latent heat flux in the HIGHTSI model with the corresponding observations, and (c) the comparison of the parameterized sensible heat flux by using observed surface temperature with observations.

approximately once a week. It should be noted that although the measurement depth of T_{os} is not fixed, the sea-water temperature shows little variation with depth in the oceanic surface layer where the measurement of T_{os} is conducted. To match the time step of 30 min for the model input, continuous daily $T_{os} - T_w$ data are first generated through smoothing the observed $T_{os} - T_w$ with moving average method. Then, the Q_w scheme based on Eqn (7) is used to force the HIGHTSI model, and the value of k_c in Eqn (7) is tested within the range from 0 to $50 \text{ W m}^{-2} \text{ } ^\circ\text{C}^{-1}$ with a step of $0.1 \text{ W m}^{-2} \text{ } ^\circ\text{C}^{-1}$. These experiments indicate the optimum k_c of $21.8 \text{ W m}^{-2} \text{ } ^\circ\text{C}^{-1}$. Figure 12b exhibits the simulated sea-ice thickness by the model forced by measurements of U , T_a , R_h , C_n and h_s , plus measurements of all the upper interface fluxes when k_c is set as $21.8 \text{ W m}^{-2} \text{ } ^\circ\text{C}^{-1}$. It can be found that the simulated sea-ice thickness is in good agreement with the observations, and the smallest mean *bias* of 0.05 m is obtained when k_c is set as $21.8 \text{ W m}^{-2} \text{ } ^\circ\text{C}^{-1}$.

Figure 12b also shows the corresponding time series of Q_w , which clearly exhibits a seasonal variation characterized by a decrease from 7.5 W m^{-2} at the beginning of the observation period to 0.9 W m^{-2} at the end. The seasonal variation of Q_w reflects

the seasonal variation of sea-water temperature, which is related to the water masses advected along the shelf (Heil and others, 1996). Some previous studies reported the similar Q_w value to our results. For example, Heil and others (1996) found that Q_w was $<2 \text{ W m}^{-2}$ during the period from early July to late November in the Prydz Bay region; Lei and others (2010) indicated that Q_w decreased from $11.8 (\pm 3.5) \text{ W m}^{-2}$ in April to $1.9 (\pm 2.4) \text{ W m}^{-2}$ in September at Zhongshan station. However, some studies also show that Q_w exhibits significant interannual and spatial variability (Heil and others, 1996; Perovich and Elder, 2002; Kirillov and others, 2015). In addition, a similar seasonal variation pattern of Q_w was reported by Yang and others (2016a). However, although Yang and others (2016a) also used the HIGHTSI model combined with observed sea-ice thicknesses to derive Q_w near Zhongshan station, they reported that Q_w decreased from 20 to 5 W m^{-2} during the same season as our experiment. A possible explanation is that they used U , T_a , R_h , C_n and P only to force the HIGHTSI model; that is, the thermodynamic processes at the upper boundary were parameterized. In contrast, in our study, to reduce the errors caused by parameterization schemes at the upper boundary, the observed surface energy fluxes are used to force the HIGHTSI model.

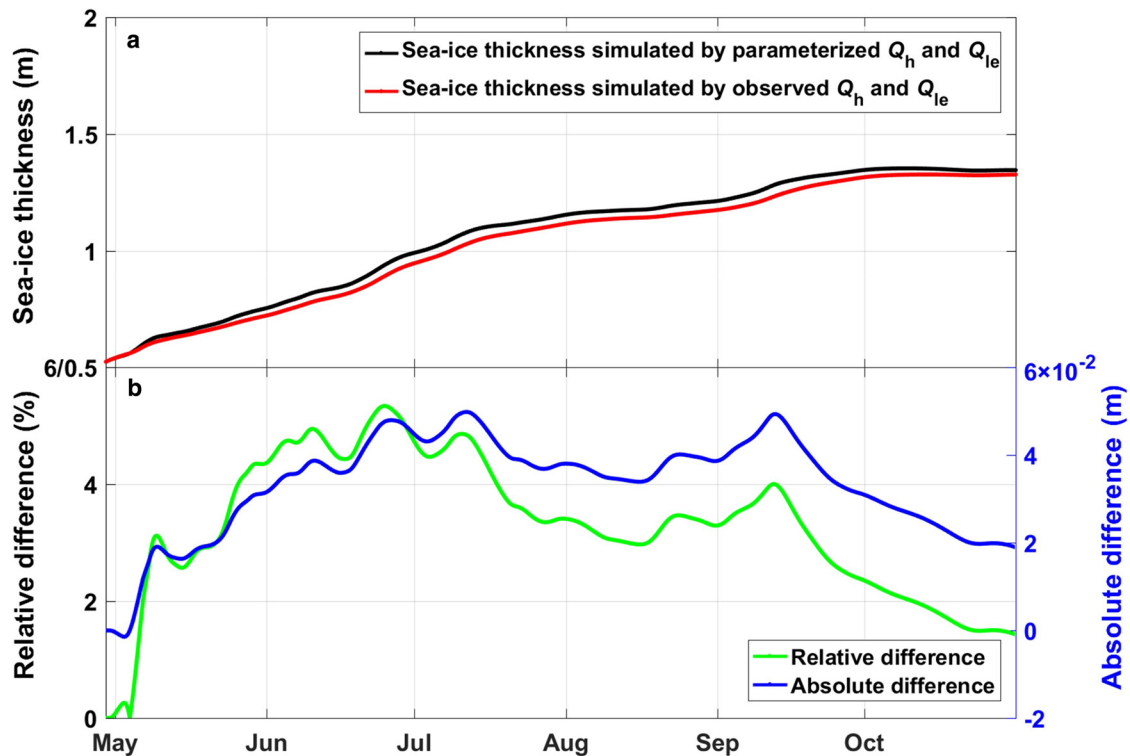


Fig. 10. (a) Sea-ice thickness simulated by the parameterized sensible heat flux and latent heat flux (black line) and that simulated by the observed sensible heat flux and latent heat flux (red line) and (b) their relative (green line, scaled to the left y axis) and absolute (blue line, scaled to the right y axis) differences.

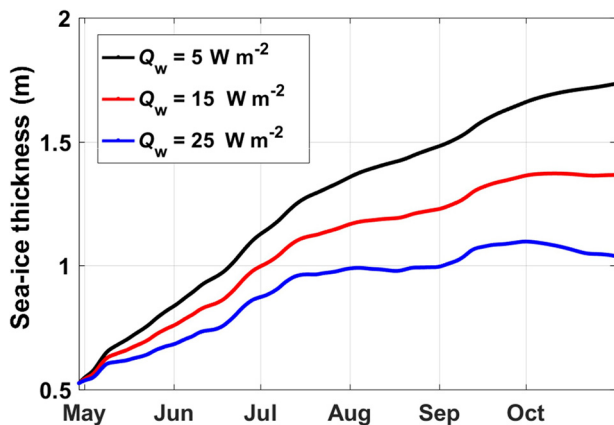


Fig. 11. Simulated sea-ice thickness with the oceanic heat flux setting as 5 W m^{-2} (black line), 15 W m^{-2} (red line) and 25 W m^{-2} (blue line).

Furthermore, by using surface temperature and sea-ice thickness observations to solve the thermal energy balance equation at the bottom of sea ice (named the heat residual method), Zhao and others (2019) discovered that the monthly mean Q_w in May was 27 W m^{-2} and fell to $\sim 10 \text{ W m}^{-2}$ after July. Compared with the method used in our study, the heat residual method is simpler; nevertheless, the heat residual method produces a periodic 1- to 2-month oscillation (Lei and others, 2010; Zhao and others, 2019). Hence, the heat residual method may be less reliable because it produces a spurious oscillation.

On the other hand, to verify the applicability of new Q_w parameterization scheme, the U , T_a , R_{lh} , C_n and h_s data collected at the same site during the period from 29 April to 31 October in 2017, and the calculated Q_w by using the formula of $k_c \times (T_{os} - T_w)$ with $k_c = 21.8 \text{ W m}^{-2} \text{ }^\circ\text{C}^{-1}$ is used to force the HIGHTSI model. Due to the lack of reliable measurements of the upper interface fluxes in 2017, the thermodynamic processes are

parameterized in the HIGHTSI model and the choices of parameterization schemes are based on our evaluation results. As shown in Fig. 13a, the calculated Q_w decreases from 9.9 W m^{-2} at the beginning of observation period to the minimum of 1.5 W m^{-2} on 5 October 2017, and it shows a slight increase in trend after 5 October 2017. By using this calculated Q_w to force the HIGHTSI model, the simulated sea-ice thickness shows good agreement with the observations, however, the simulated sea-ice thickness simulated by the constant Q_w of 15 W m^{-2} is significantly underestimated compared with the observations (Fig. 13b). Hence, these results indicate that the new parameterization scheme of Q_w is useful across two seasons at Prydz Bay. Compared with the calculated Q_w in 2016, the calculated Q_w in 2017 looks to be a different magnitude across both years by 25%, but the new parameterization scheme still works well. Furthermore, the best parameterization in 2016 also works well in 2017, which indicates the robustness of the new parameterization.

It should be noted that our study presents a constant k_c , however, as demonstrated in Section 2.4, k_c should be related to the current velocity, which exists a daily variation (Jenkins and others, 2010). In addition, the T_w , which is set as a constant of -1.8°C in this study, should depend on the salinity of the underlying sea water (Vancoppenolle and others, 2019) and the settings of T_w will also have impacts on k_c . Hence, the representativeness of k_c we presented may be limited to the local scale and the temporal variation characteristic of k_c is lost. To develop a more realistic Q_w parameterization scheme, the measurements of current velocity, salinity, as well as some turbulent parameters in the oceanic surface layer are still required.

3.6 Seasonal variation in the heat budget and its influence on the sea-ice thickness variation

The monthly mean net shortwave radiation $Q_s(1 - \alpha) - I_0$, net longwave radiation $(Q_d - Q_b)$, Q_h , Q_{le} , Q_c , $F(T_s)$, Q_w and the

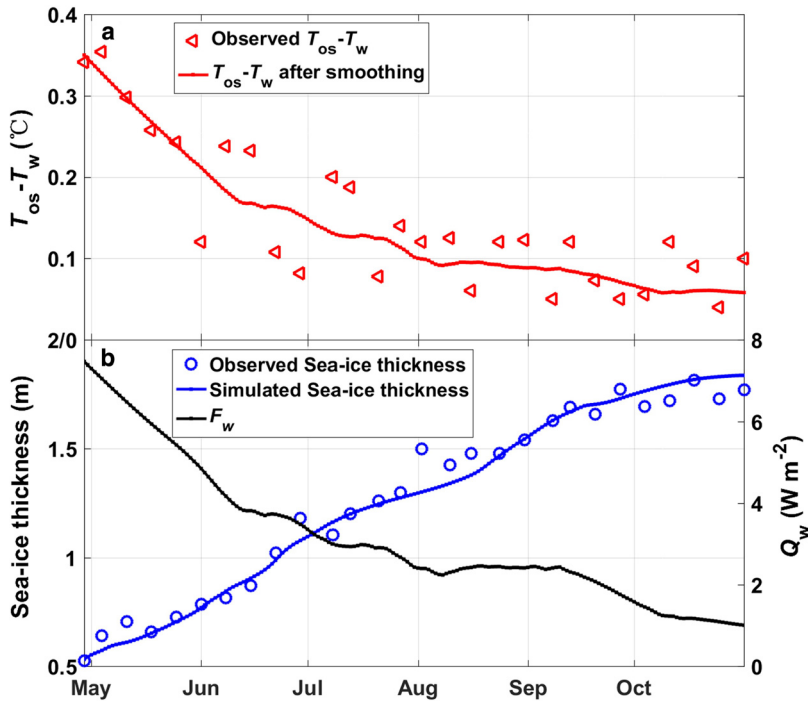


Fig. 12. (a) Observed $T_{os} - T_w$ (red triangle) and smoothed result (red line), and (b) the observed sea-ice thickness (blue circle), simulated sea-ice thickness with $k_c = 21.8 W m^{-2} \text{ } ^\circ C^{-1}$ (blue line), and the corresponding oceanic heat flux (black line) in 2016.

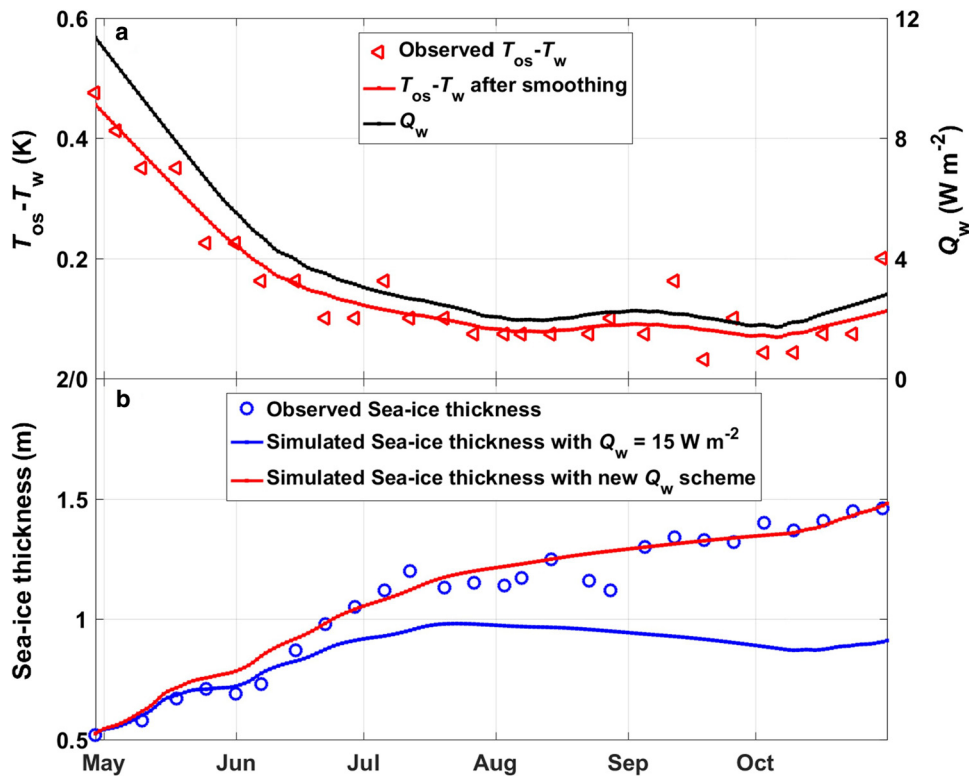


Fig. 13. (a) Observed (red triangle) and smoothed (red line) $T_{os} - T_w$, and the calculated oceanic heat flux Q_w by $k_c \times (T_{os} - T_w)$ with $k_c = 21.8 W m^{-2} \text{ } ^\circ C^{-1}$ (black line), and (b) the comparison between observed sea-ice thickness (blue circle) and simulated sea-ice thickness with $Q_w = 15 W m^{-2}$ (blue line) and $Q_w = k_c \times (T_{os} - T_w)$ with $k_c = 21.8 W m^{-2} \text{ } ^\circ C^{-1}$ (red line) in 2017.

monthly growth of sea-ice thickness are presented in Table 4. These values are calculated from the results of modeling experiment, which is driven by the observed surface heat fluxes and with best choice of K_c . It can be found that the net shortwave radiation, Q_h , and Q_c are the heat sources at the snow surface, while the net longwave radiation and Q_{le} are the heat sinks at the snow surface during the growth season. From May to September, the

surface loses energy to atmosphere through radiation fluxes, mainly due to a negative net longwave radiation, while Q_h and Q_c become the leading heat source. The monthly mean Q_w gradually decreases from $6.2 W m^{-2}$ in May to $1.2 W m^{-2}$ in October, and the value of the monthly mean Q_w is small compared with the other terms. Among these heat budget terms, the seasonal variation in the net shortwave radiation is the most significant,

Table 4. Monthly mean heat fluxes and sea-ice thickness from May to October and their std dev values as calculated from model tuning results.

	Month					
	May	June	July	August	September	October
$Q_s(1 - \alpha) - I_0$ ($W m^{-2}$)	0.4 ± 2.8	0.0 ± 0.0	0.1 ± 0.9	2.9 ± 8.0	14.7 ± 22.0	39.8 ± 43.1
$(Q_d - Q_b)$ ($W m^{-2}$)	-43.6 ± 23.7	-37.1 ± 28.2	-24.4 ± 22.2	-57.2 ± 27.8	-48.2 ± 33.8	-53.8 ± 31.3
Q_h ($W m^{-2}$)	26.6 ± 19.2	13.3 ± 16.9	22.0 ± 20.7	38.9 ± 23.4	24.3 ± 24.1	21.0 ± 19.9
Q_{le} ($W m^{-2}$)	-9.2 ± 12.0	-4.4 ± 5.9	-4.7 ± 8.1	-9.5 ± 12.5	-5.9 ± 9.2	-10.6 ± 9.5
Q_c ($W m^{-2}$)	25.5 ± 19.5	28.2 ± 11.3	7.1 ± 12.5	24.6 ± 11.0	15.0 ± 15.6	3.6 ± 15.6
$F(T_s)$ ($W m^{-2}$)	-0.2 ± 2.3	0 ± 2.3	0.3 ± 2.7	-0.2 ± 2.3	0 ± 2.1	0.7 ± 1.7
Q_w ($W m^{-2}$)	6.2 ± 0.7	4.0 ± 0.4	2.9 ± 0.2	2.4 ± 0.1	2.2 ± 0.3	1.2 ± 0.1
$(dh_{si}/dt)_{tot}$ ($m month^{-1}$)	0.22 ± 0.06	0.33 ± 0.1	0.19 ± 0.05	0.26 ± 0.08	0.21 ± 0.06	0.08 ± 0.04

increasing from $0 W m^{-2}$ in June to $39.8 W m^{-2}$ in October. It can also be found that the larger Q_c and the smaller Q_w will intensify the growth of the sea-ice bottom. For example, the Q_w in August is similar to that in September, however, the Q_c in August is $9.6 W m^{-2}$ larger than that in September, which leads to the more sea-ice growth in August. In October, the significantly reduced Q_c leads to the minimum of sea-ice growth. In addition, although the Q_c in August is close to that in May, caused by the smaller Q_w in August, the sea-ice growth in August is larger than that in May. Hence, this case indicates the smaller Q_w is conducive to the growth of the sea ice. Table 4 also presents the monthly mean net flux, which is assumed to be equal to $0 W m^{-2}$ in the calculation of surface temperature. It is clear that the model results agree with the assumption of $F(T_s) = 0 W m^{-2}$ under freezing conditions.

4. Summary

By using data collected throughout the sea-ice growth season over the landfast sea ice in Prydz Bay, East Antarctica, the parameterization schemes of thermodynamic processes at the upper sea-ice boundary in the HIGHTSI model are examined, and we propose a modified oceanic heat flux (Q_w) parameterization scheme.

Comparing the results of solar radiation (Q_s), albedo (α), downward longwave radiation (Q_d), upward longwave radiation (Q_b), sensible heat flux (Q_h) and latent heat flux (Q_{le}) from the parameterization schemes with the corresponding observations reveals that the surface turbulent flux parameterization schemes produce the largest deviations from the observations. However, although the parameterized Q_h and Q_{le} present the largest deviations from the observations, the influence of this deviation on the sea-ice thickness simulation is not the most significant. At the upper sea-ice boundary, the differences between the parameterized and observed Q_b tend to have the greatest influence on the simulated sea-ice thickness. In addition, our results suggest that the best choices for the α and Q_d parameterization schemes in the HIGHTSI model are the HadCM3 scheme and Id81 scheme, respectively. Furthermore, the simulated sea-ice thickness is very sensitive to Q_w during the sea-ice growth season. Hence, it is important to select a reasonable Q_w parameterization scheme in the HIGHTSI model. In the current study, a modified scheme of $k_c \times (T_{os} - T_w)$ with $k_c = 21.8 W m^{-2} \text{ } ^\circ C^{-1}$ is proposed. This scheme also works well for an independent verification in a different year.

Finally, the seasonal variation in the heat budget and its influence on the sea-ice thickness variation are also discussed in this study. The net shortwave radiation and Q_h are found to be the heat sources at the surface during the growth season, while the net longwave radiation and Q_{le} are the heat sinks at the surface. The larger conductive heat flux and the smaller oceanic heat flux are conducive to intensify the growth of the sea-ice.

This study helps us to improve understanding of the thermodynamic processes of sea ice and our results provide a reference for the choice of parameterization scheme of thermodynamic processes. However, it should be noted that this study only focuses on the simulation of sea-ice thickness during the sea-ice growth season due to the limitation of observation data, while it is also important to investigate the simulation of sea-ice thickness during the melting season. In addition, our data were collected at a single observation site in Prydz Bay, East Antarctica, the representativeness of our results may be limited to the very local area. To overcome this limitation, the international joint efforts on the Antarctic landfast sea-ice observations are strongly required (e.g. Heil and others, 2011).

Acknowledgements. This study was supported by the National Natural Science Foundation of China (nos. 41941009, 41922044, 42105072 and 41876212), the Guangdong Basic and Applied Basic Research Foundation (nos. 2020B1515020025, 2021A1515011591 and 2021A1515012209), the China Postdoctoral Science Foundation (no. 2021M693585), the Fundamental Research Funds for the Central Universities, Sun Yat-sen University (nos. 19lgzd07 and 2021qntd29), the Southern Marine Science and Engineering Guangdong Laboratory (Zhuhai) (SML2020SP007) and the Academy of Finland (contract 304345). We thank the Chinese Arctic and Antarctic Administration and Polar Research Institute of China for logistic support. We also thank the Russian Progress II meteorological station for providing the precipitation data.

Author contributions. Changwei Liu performed all calculations and wrote the first draft, Qinghua Yang made many constructive suggestions and helped improve the manuscript, Guanghua Hao provided the most of data and also gave some helpful suggestions, Yubin Li, Jiechen Zhao, Ruibo Lei, Bin Cheng and Zhiqiu Gao helped revise the manuscript.

References

- Ackley SF, Xie H and Tichenor EA (2015) Ocean heat flux under Antarctic sea ice in the Bellingshausen and Amundsen seas: two case studies. *Annals of Glaciology* **56**(69), 200–210. doi: [10.3189/2015AoG69A890](https://doi.org/10.3189/2015AoG69A890)
- Andreas EL (1987) A theory for the scalar roughness and the scalar transfer coefficients over snow and sea ice. *Boundary-Layer Meteorology* **38**(1), 159–184. doi: [10.1007/BF00121562](https://doi.org/10.1007/BF00121562)
- Andreas EL and Ackley SF (1982) On the difference in ablation seasons of Arctic and Antarctic sea ice. *Journal of the Atmospheric Sciences* **39**, 440–447. doi: [10.1175/1520-0469\(1982\)039<0392.0.CO;2](https://doi.org/10.1175/1520-0469(1982)039<0392.0.CO;2)
- Banke EG, Smith SD and Anderson RJ (1980) Drag coefficient at AIDJEX from sonic anemometer measurement. In Pritchard RS (ed.), *Sea-Ice Processes and Models*. Seattle: University of Washington Press, pp. 430–442.
- Bennett TJ (1982) A coupled atmosphere-sea-ice model study of the role of sea-ice in climatic predictability. *Journal of the Atmospheric Sciences* **39**, 1456–1465. doi: [10.1175/1520-0469\(1982\)039<1456:acasim>2.0.co;2](https://doi.org/10.1175/1520-0469(1982)039<1456:acasim>2.0.co;2)
- Briegleb BP and 6 others (2004) Scientific description of the sea ice component in the community climate system model, version 3. NCAR/TN-463 + STR.
- Brustaert W (1975) On a derivable formula for longwave radiation from clear skies. *Water Resources Research* **11**, 742–744. doi: [10.1029/WR011i005p00742](https://doi.org/10.1029/WR011i005p00742)

- Cheng B, Mäkynen M, Similä M, Rontu L and Vihma T** (2013) Modelling snow and ice thickness in the coastal Kara Sea, Russian Arctic. *Annals of Glaciology* **54**(62), 105–113. doi: [10.1389/2013AoG62A180](https://doi.org/10.1389/2013AoG62A180)
- Dethloff K and 5 others** (1996) Regional climate model of the Arctic atmosphere. *Journal of Geophysical Research* **101**(D18), 23401–23422. doi: [10.1029/96jd02016](https://doi.org/10.1029/96jd02016)
- Dumas J, Carmack E and Melliing H** (2005) Climate change impacts on the Beaufort shelf landfast ice. *Cold Regions Science and Technology* **42**, 41–51. doi: [10.1016/j.coldregions.2004.12.001](https://doi.org/10.1016/j.coldregions.2004.12.001)
- Efimova NA** (1961) On methods of calculating monthly values of net long-wave radiation. *Meteorologiya i Gidrologiya* **10**, 28–33.
- Flato GM and Brown RD** (1996) Variability and climate sensitivity of landfast Arctic sea ice. *Journal of Geophysical Research* **101**(C11), 25767–25777. doi: [10.1029/96jc02431](https://doi.org/10.1029/96jc02431)
- Fraser AD, Massom RA, Michael KJ, Galton-Fenzi BK and Lieser JL** (2012) East Antarctic landfast sea ice distribution and variability, 2000–08. *Journal of Climate* **25**(4), 1137–1156. doi: [10.1175/JCLI-D-10-05032.1](https://doi.org/10.1175/JCLI-D-10-05032.1)
- Giles KA, Laxon SW and Ridout AL** (2008) Circumpolar thinning of Arctic sea ice following the 2007 record ice extent minimum. *Geophysical Research Letters* **35**, L22502. doi: [10.1029/2008GL035710](https://doi.org/10.1029/2008GL035710)
- Gordon C and 7 others** (2000) The simulation of SST, sea ice extents and ocean heat transports in a version of the Hadley Centre coupled model without flux adjustments. *Climate Dynamics* **16**, 147–168. doi: [10.1007/s003820050010](https://doi.org/10.1007/s003820050010)
- Gordon AL and Huber BA** (1990) Southern ocean winter mixed layer. *Journal of Geophysical Research: Oceans* **95**(C7), 11655–11672. doi: [10.1029/JC095iC07p11655](https://doi.org/10.1029/JC095iC07p11655)
- Guest PS** (1998) Surface longwave radiation conditions in the eastern Weddell Sea during winter. *Journal of Geophysical Research* **103**(C13), 30761–30771. doi: [10.1029/98jc02146](https://doi.org/10.1029/98jc02146)
- Hao G, Pirazzini R, Yang Q, Tian Z and Liu C** (2020) Spectral albedo of coastal landfast sea ice in Prydz Bay, Antarctica. *Journal of Glaciology* **67** (261), 1–11. doi: [10.1017/jog.2020.90](https://doi.org/10.1017/jog.2020.90)
- Heil P** (2006) Atmospheric conditions and fast ice at Davis, East Antarctica: a case study. *Journal of Geophysical Research: Oceans* **111**, C05009. doi: [10.1029/2005JC002904](https://doi.org/10.1029/2005JC002904)
- Heil P, Allison I and Lytle VI** (1996) Seasonal and interannual variations of the oceanic heat flux under a landfast Antarctic ice cover. *Journal of Geophysical Research: Oceans* **101**(C11), 25741–25752. doi: [10.1029/96JC01921](https://doi.org/10.1029/96JC01921)
- Heil P, Gerland S and Granskog MA** (2011) An Antarctic monitoring initiative for fast ice and comparison with the Arctic. *The Cryosphere Discussions* **5**, 2437–2463. doi: [10.5194/tcd-5-2437-2011](https://doi.org/10.5194/tcd-5-2437-2011)
- Hibler WD** (1979) A dynamic thermodynamic sea ice model. *Journal of Physical Oceanography* **9**, 815–846. doi: [10.1175/1520-0485\(1979\)009<0815:adtsim>2.0.co;2](https://doi.org/10.1175/1520-0485(1979)009<0815:adtsim>2.0.co;2)
- Idso SB** (1981) A set of equations for full spectrum and 8–14 microns and 10.5–12.5 microns thermal radiation from cloudless skies. *Water Resources Research* **17**, 295–304. doi: [10.1029/WR017i002p00295](https://doi.org/10.1029/WR017i002p00295)
- Idso SB and Jackson RD** (1969) Thermal radiation from the atmosphere. *Journal of Geophysical Research* **74**(23), 5397–5403. doi: [10.1029/JC074i023p05397](https://doi.org/10.1029/JC074i023p05397)
- Jacob D and 15 others** (2001) A comprehensive model intercomparison study investigating the water budget during the BALTEX-PIDCAP period. *Meteorology and Atmospheric Physics* **77**, 19–43. doi: [10.1007/s007030170015](https://doi.org/10.1007/s007030170015)
- Jacobs JD** (1978) Radiation climate of Broughton Island. In: Barry, R. G., J. D., Jacobs (Eds.). *Energy Budget Studies in Relation to Fast-ice Breakup Processes in Davis Strait*, CCAS Pap., 26: 105–120, Inst. of Arctic and Alp. Res., Univ. of Colorado, Boulder, CO.
- Jenkins A, Nicholls K and Corr H** (2010) Observation and parameterization of ablation at the base of Ronne ice shelf, Antarctica. *Journal of Physical Oceanography* **40**, 2298–2312. doi: [10.1175/2010JPO4317.1](https://doi.org/10.1175/2010JPO4317.1)
- Key JR, Silcox RA and Stone RS** (1996) Evaluation of surface radiative flux parameterizations for use in sea ice models. *Journal of Geophysical Research: Oceans* **101**, 3839–3849. doi: [10.1029/95JC03600](https://doi.org/10.1029/95JC03600)
- Kirilov SA, Dmitrenko I, Babb D, Rysgaard S and Barber D** (2015) The effect of ocean heat flux on seasonal ice growth in Yong sound (Northeast Greenland). *Journal of Geophysical Research: Oceans* **120**(7), 4803–4824. doi: [10.1002/2015JC010720](https://doi.org/10.1002/2015JC010720)
- Kuzmin PP** (1961) *Process of Snow Cover Melting*. Leningrad: Gidrometeoizdat (in Russian).
- Launiainen J and Cheng B** (1995) A simple noniterative algorithm for calculating turbulent bulk fluxes in diabatic conditions over water, snow and ground surface. Rep. Series in Geophys. 33. Dept. of Geophys., Univ. of Helsinki.
- Launiainen J and Cheng B** (1998) Modelling of ice thermodynamics in natural water bodies. *Cold Regions Science and Technology* **27**, 153–178. doi: [10.1016/S0165-232X\(98\)00009-3](https://doi.org/10.1016/S0165-232X(98)00009-3)
- Lei R, Li Z, Cheng B, Zhang Z and Heil P** (2010) Annual cycle of landfast sea ice in Prydz Bay, east Antarctica. *Journal of Geophysical Research: Oceans* **115**, C02006. doi: [10.1029/2008JC005223](https://doi.org/10.1029/2008JC005223)
- Liu C and 9 others** (2020) Measurements of turbulence transfer in the near-surface layer over the Antarctic sea-ice surface from April through November in 2016. *Annals of Glaciology* **61**(82), 1–12. doi: [10.1017/aog.2019.48](https://doi.org/10.1017/aog.2019.48)
- Lynch AH, Chapman WL, Walsh JE and Weller G** (1995) Development of a regional climate model of the western Arctic. *Journal of Climate* **8**(6), 1555–1570. doi: [10.1175/1520-0442\(1995\)008<1555:doarcm>2.0.co;2](https://doi.org/10.1175/1520-0442(1995)008<1555:doarcm>2.0.co;2)
- Maykut GA and Church PE** (1973) Radiation climate of Barrow, Alaska, 1962–1966. *Journal of Applied Meteorology and Climatology* **12**, 620–628. doi: [10.1175/1520-0450\(1973\)0122.0.CO;2](https://doi.org/10.1175/1520-0450(1973)0122.0.CO;2)
- Maykut GA and Untersteiner N** (1971) Some results from a time dependent thermodynamic model of sea-ice. *Journal of Geophysical Research* **76**(6), 1550–1575. doi: [10.1029/JC076i006p01550](https://doi.org/10.1029/JC076i006p01550)
- McPhee M, Kottmeier C and Morison J** (1999) Ocean heat flux in the central Weddell Sea during winter. *Journal of Physical Oceanography* **29**, 1166–1179. doi: [10.1175/1520-0485\(1999\)029<1166:OHFITC>2.0.CO;2](https://doi.org/10.1175/1520-0485(1999)029<1166:OHFITC>2.0.CO;2)
- Merkouriadi I, Cheng B, Graham RM, Rösel A and Granskog MA** (2017) Critical role of snow on sea ice growth in the Atlantic sector of the Arctic ocean. *Geophysical Research Letters* **44**(20), 10479–10485. doi: [10.1002/2017GL075494](https://doi.org/10.1002/2017GL075494)
- Merkouriadi I, Cheng B, Hudson SR and Granskog MA** (2020) Effect of frequent winter warming events (storms) and snow on sea ice growth – a case from the Atlantic sector of the Arctic Ocean during the N-ICE2015 campaign. *Annals of Glaciology* **61**(82), 164–170. doi: [10.1017/aog.2020.25](https://doi.org/10.1017/aog.2020.25)
- Ohmura A** (1981) Climate and energy balance of the Arctic tundra. Zürcher Geogr. Schr. 3, 448, Geogr. Inst., Zürich, Switzerland.
- Parkinson CL and Washington WM** (1979) A large-scale numerical model of sea-ice. *Journal of Geophysical Research* **84**(C1), 311–337. doi: [10.1029/JC084iC01p00311](https://doi.org/10.1029/JC084iC01p00311)
- Perovich DK** (1996) The optical properties of sea-ice. Cold Reg. Res. and Eng. Lab. (CRREL), Report 96–1, Hanover, NH.
- Perovich DK and Elder B** (2002) Estimates of ocean heat flux at SHEBA. *Geophysical Research Letters* **29**(9), 1344. doi: [10.1029/2001GL014171](https://doi.org/10.1029/2001GL014171)
- Prata AJ** (1996) A new longwave formula for estimating downward clear-sky radiation at the surface. *Quarterly Journal of the Royal Meteorological Society* **122**, 1127–1151. doi: [10.1002/qj.49712253306](https://doi.org/10.1002/qj.49712253306)
- Satterlund DR** (1979) An improved equation for estimating longwave radiation from the atmosphere. *Water Resources Research* **15**(6), 1649–1650. doi: [10.1029/WR015i006p01649](https://doi.org/10.1029/WR015i006p01649)
- Shine KP** (1984) Parameterization of shortwave flux over high albedo surfaces as a function of cloud thickness and surface albedo. *Quarterly Journal of the Royal Meteorological Society* **110**, 747–764. doi: [10.1002/qj.49711046511](https://doi.org/10.1002/qj.49711046511)
- Shu Q and 6 others** (2020) Assessment of sea ice extent in CMIP6 with comparison to observations and CMIP5. *Geophysical Research Letters* **47**(9), e2020GL087965. doi: [10.1029/2020GL087965](https://doi.org/10.1029/2020GL087965)
- Sturm M, Holmgren J, König M and Morris K** (1997) The thermal conductivity of seasonal snow. *Journal of Glaciology* **43**, 26–41. doi: [10.1017/S002214300002781](https://doi.org/10.1017/S002214300002781)
- Swinbank WC** (1963) Longwave radiation from clear skies. *Quarterly Journal of the Royal Meteorological Society* **89**, 339–348. doi: [10.1002/qj.49708938105](https://doi.org/10.1002/qj.49708938105)
- Tang S, Qin D, Ren J and Kang J** (2006) Sea ice characteristics between middle Weddell Sea and Prydz Bay, Antarctic during the 2003 Australian summer. *Frontiers of Earth Science* **13**(3), 213–218 (in Chinese). doi: [10.1016/S1001-8042\(06\)60021-3](https://doi.org/10.1016/S1001-8042(06)60021-3)
- Turner J and Comiso J** (2017) Solve Antarctica's sea-ice puzzle. *Nature* **547**, 275–277. doi: [10.1038/547275a](https://doi.org/10.1038/547275a)
- Vancoppenolle M and 5 others** (2009) Simulating the mass balance and salinity of Arctic and Antarctic sea ice: 1. Model description and validation. *Ocean Modelling* **27**, 33–53. doi: [10.1016/j.oceanmod.2008.10.005](https://doi.org/10.1016/j.oceanmod.2008.10.005)
- Vancoppenolle M, Madec G, Thomas M and McDougall TJ** (2019) Thermodynamics of sea ice phase composition revisited. *Journal of Geophysical Research: Oceans* **124**, 615–634. doi: [10.1029/2018JC014611](https://doi.org/10.1029/2018JC014611)

- Vihma T, Johansson MM and Launiainen J** (2009) Radiative and turbulent surface heat fluxes over sea ice in the western Weddell Sea in early summer. *Journal of Geophysical Research* **114**, C04019. doi: [10.1029/2008JC004995](https://doi.org/10.1029/2008JC004995)
- Williams G and 6 others** (2014) Thick and deformed Antarctic sea ice mapped with autonomous underwater vehicles. *Nature Geoscience* **8**, 61–67. doi: [10.1038/ngeo2299](https://doi.org/10.1038/ngeo2299)
- Yang Y and 5 others** (2016a) Modelling the thickness of landfast sea ice in Prydz Bay, East Antarctica. *Antarctic Science* **28**(01), 59–70. doi: [10.1017/S0954102015000449](https://doi.org/10.1017/S0954102015000449)
- Yang Q and 9 others** (2016b) Albedo of coastal landfast sea ice in Prydz Bay, Antarctica: observations and parameterization. *Advances in Atmospheric Sciences* **33**, 535–543. doi: [10.1007/s00376-015-5114-7](https://doi.org/10.1007/s00376-015-5114-7)
- Zhao J and 10 others** (2019) Spatial and temporal evolution of landfast ice near Zhongshan station, east Antarctica, over an annual cycle in 2011/2012. *Acta Oceanologica Sinica* **38**(5), 51–61. doi: [10.1007/s13131-018-1339-5](https://doi.org/10.1007/s13131-018-1339-5)
- Zhao J, Cheng B, Yang Q, Vihma T and Zhang L** (2017) Observations and modelling of first-year ice growth and simultaneous second-year ice ablation in the Prydz Bay, East Antarctica. *Annals of Glaciology* **58**(75pt1), 59–67. doi: [10.1017/aog.2017.33](https://doi.org/10.1017/aog.2017.33)